ACS APPLIED MATERIALS & INTERFACES

www.acsami.org

Research Article

CXCR4-Targeted Macrophage-Derived Biomimetic Hybrid Vesicle Nanoplatform for Enhanced Cancer Therapy through Codelivery of Manganese and Doxorubicin

Yeonwoo Jang,[⊥] Young Seok Cho,[⊥] April Kim, Xingwu Zhou, Yujin Kim, Ziye Wan, James J. Moon,* and Hansoo Park*

Cite This: *ACS Appl. Mater. Interfaces* 2024, 16, 17129−17144

Read Online

ACCESS | Metrics & More | Article Recommendations | Supporting Information

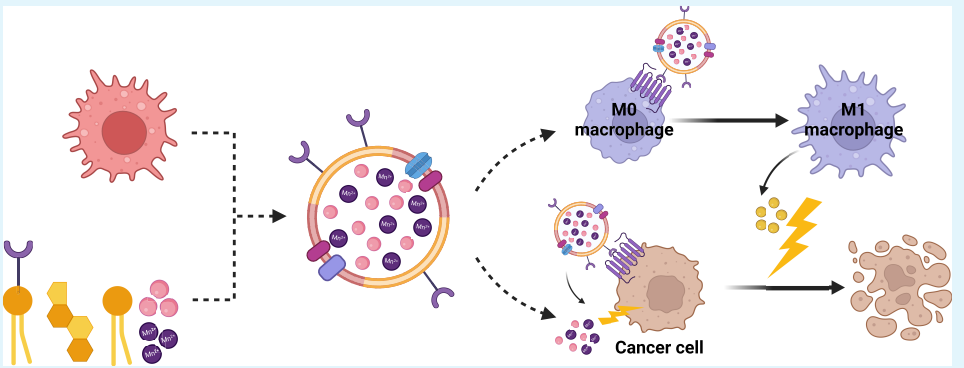

ABSTRACT: Immune-cell-derived membranes have garnered significant attention as innovative delivery modalities in cancer immunotherapy for their intrinsic immune-modulating functionalities and superior biocompatibilities. Integrating additional parental cell membranes or synthetic lipid vesicles into cellular vesicles can further potentiate their capacities to perform combinatorial pharmacological activities in activating antitumor immunity, thus providing insights into the potential of hybrid cellular vesicles as versatile delivery vehicles for cancer immunotherapy. Here, we have developed a macrophage-membrane-derived hybrid vesicle that has the dual functions of transporting immunotherapeutic drugs and shaping the polarization of tumor-associated macrophages for cancer immunotherapy. The platform combines M1 macrophage-membrane-derived vesicles with CXCR4-binding-peptide-conjugated liposomes loaded with manganese and doxorubicin. The hybrid nanovesicles exhibited remarkable macrophage-targeting capacity through the CXCR4-binding peptide, resulting in enhanced macrophage polarization to the antitumoral M1 phenotype characterized by proinflammatory cytokine release. The manganese/doxorubicin-loaded hybrid vesicles in the CXCR4-expressing tumor cells evoked potent cancer cytotoxicity, immunogenic cell death of tumor cells, and STING activation. Moreover, cotreatment with manganese and doxorubicin promoted dendritic cell maturation, enabling effective tumor growth inhibition. In murine models of CT26 colon carcinoma and 4T1 breast cancer, intravenous administration of the manganese/doxorubicin-loaded hybrid vesicles elicited robust tumor-suppressing activity at a low dosage without adverse systemic effects. Local administration of hybrid nanovesicles also induced an abscessive effect in a bilateral 4T1 tumor model. This study demonstrates a promising biomimetic manganese/doxorubicin-based hybrid nanovesicle platform for effective cancer immunotherapy tailored to the tumor microenvironment, which may offer an innovative approach to combinatorial immunotherapy.

KEYWORDS: *macrophage-membrane-derived vesicle, membrane engineering, biomimetic hybrid vesicle, combination therapy, cancer immunotherapy, metalloimmunotherapy*

INTRODUCTION

Cancer immunotherapy is a revolutionary approach to cancer treatment that has achieved unprecedented clinical success, but it also faces challenges, such as high variation in patient response rate, development of resistance, and susceptibility to autoimmune side effects.[1−3] Combination therapy strategies have shown promise in addressing these issues as well as achieving more comprehensive and synergistic effects for treating cancer.[4,5] Drug delivery systems (DDSs) have been

Received: December 11, 2023
Revised: March 12, 2024
Accepted: March 14, 2024
Published: March 27, 2024

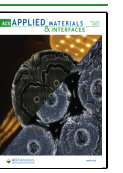

https://doi.org/10.1021/acsami.3c18569
ACS Appl. Mater. Interfaces 2024, 16, 17129−17144

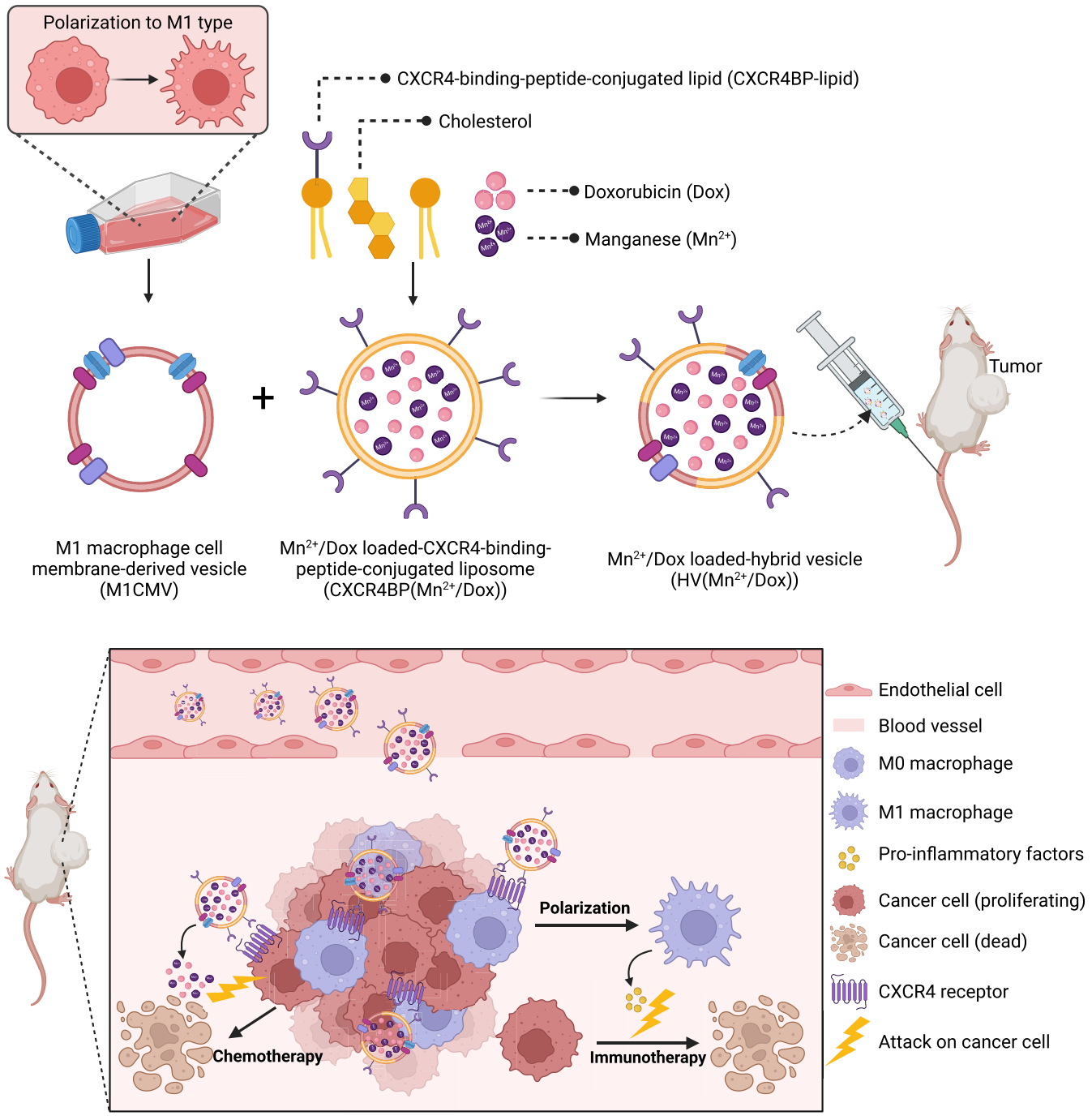

Figure 1. Schematic illustration and mode of action of a Mn^{2+}/Dox-loaded hybrid vesicle, termed HV(Mn^{2+}/Dox). Briefly, HV(Mn^{2+}/Dox) was formed by fusing M1-like macrophage-membrane-derived vesicles (M1CMVs) and CXCR4-binding-peptide-conjugated liposomes (CXCR4BPLs) carrying Mn^{2+} and Dox. HV(Mn^{2+}/Dox) allows for targeting of CXCR4-expressing cancer cells, polarization of M0-to-M1 macrophages, and secretion of proinflammatory cytokines, leading to anticancer killing and antitumor immunity.

actively exploited to improve the delivery efficiencies of multiple drugs with safe tolerability, and many recent studies have sought to develop biomimetic drug delivery platforms that exhibit great biocompatibility, targeted distribution of drugs, and enhanced effectiveness of combinatorial therapies.[6−10] Among these, biomimetic cell membranes have emerged as a new source of nanocarriers for the efficient delivery of drug cargo.[11,12] Compared with synthetic lipid or polymeric nanocarriers, cell-membrane-derived vesicles offer numerous advantages including natural biocompatibility, safe encapsulation of bioactive molecules, and intrinsic cell-to-cell interactions.

Among the emerging classes of cell membrane components, macrophage-membrane-derived vesicles (MDVs) have been widely deployed as novel DDSs owing to their multiple inherent biological properties that drive diverse functions in response to different stimuli within various pathogenic microenvironments.[13−15] Being a major messenger of the innate immune system, the macrophage membrane possesses unique immunomodulatory properties for the regulation of inflammatory responses through active intercellular communi-

https://doi.org/10.1021/acsami.3c18569
ACS Appl. Mater. Interfaces 2024, 16, 17129−17144

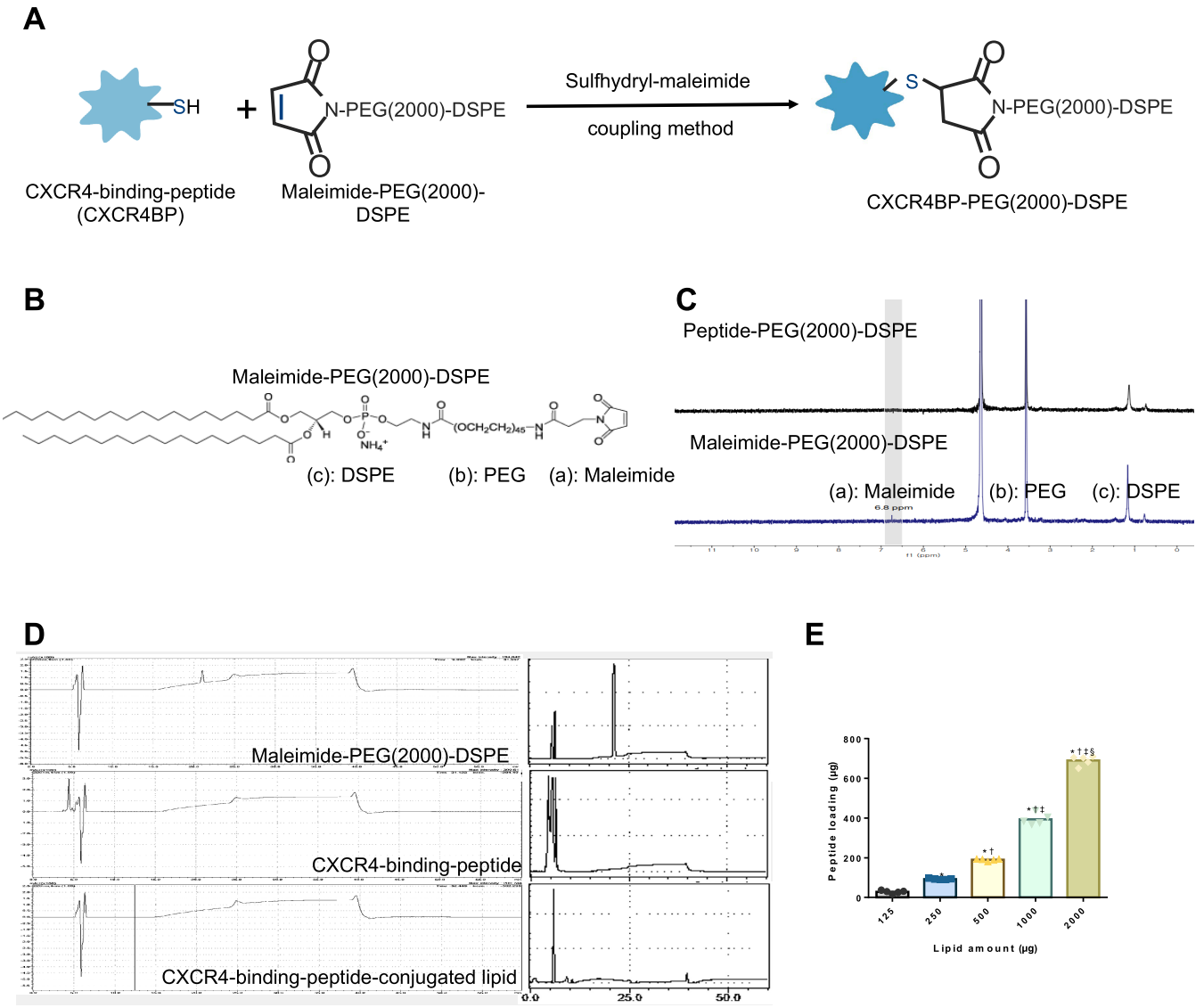

Figure 2. Synthesis and validation of CXCR4BPL. (A) Schematic illustration for the synthesis of CXCR4-binding-peptide-conjugated lipid. (B) Chemical structure of maleimide−PEG(2000)−DSPE. (C) ^{1}H NMR spectra and (D) HPLC chromatograms of maleimide−PEG(2000)−DSPE (top), CXCR4-binding peptide (middle), and CXCR4-binding-peptide-conjugated lipid (bottom). (E) Protein quantification of CXCR4BPL by BCA assay. Data represent mean ± SEM.; $n = 5$ (E) from biologically independent samples per group. $^*p < 0.05$ compared to 125 μg/mL of lipid amount, $^\dagger p < 0.05$ compared to 250 μg/mL of lipid amount, $^\ddagger p < 0.05$ compared to 500 μg/mL of lipid amount, $^\S p < 0.05$ compared to 1000 μg/mL of lipid amount (E). Data were analyzed using a one-way ANOVA with Tukey's multiple comparison test (E).

cations with both immune and tumor cells.[16] In particular, M1-like macrophage-derived membrane vesicles have attracted increasing interest in therapeutic applications against cancers for their ability to induce proinflammatory responses and promote M1-type tumor-associated macrophage polarization.[17] However, the natural homing capacities, complicated cellular structures, and phenotypic diversity introduced in MDVs are insufficient for handling the heterogeneous *in vivo* tumor microenvironment (TME).[18,19] To overcome these limitations, recent studies have focused on tailoring the cellular surfaces to confer targeting capabilities and developing complementary strategies for targeted drug delivery, such as incorporating MDVs into other targeted drug delivery vessels like ligand- or antibody-conjugated nanoparticles.[15,20−22] These hybrid nanomaterials combine the properties of both parental cell membranes and synthetic biomaterials, providing the unique advantages of mimicking natural cell functionality and enhancing target-specific delivery of drug cargo.

Additionally, the selection of an appropriate therapeutic agent is crucial in cancer immunotherapy to harness the patient's immune system effectively and maximize tumor-cell death. In the context of cancer immunotherapy, immunogenic cell death (ICD) is a key regulatory pathway in which damage-associated molecular patterns (DAMPs) released from dying cells function as danger signals to stimulate immune responses for antitumor activities. Some chemotherapeutic drugs, such as doxorubicin (Dox) and oxaliplatin (OXA), have been widely used in cancer immunotherapy for their ability to induce ICD-related immunogenicity, which makes these drugs attractive components in combination therapies.[23−25] Recently, as an alternative to conventional therapeutic modalities, metal-loimmunotherapy has been explored extensively as a potential strategy to activate host immunity by supplementing the TME

https://doi.org/10.1021/acsami.3c18569
ACS Appl. Mater. Interfaces 2024, 16, 17129−17144

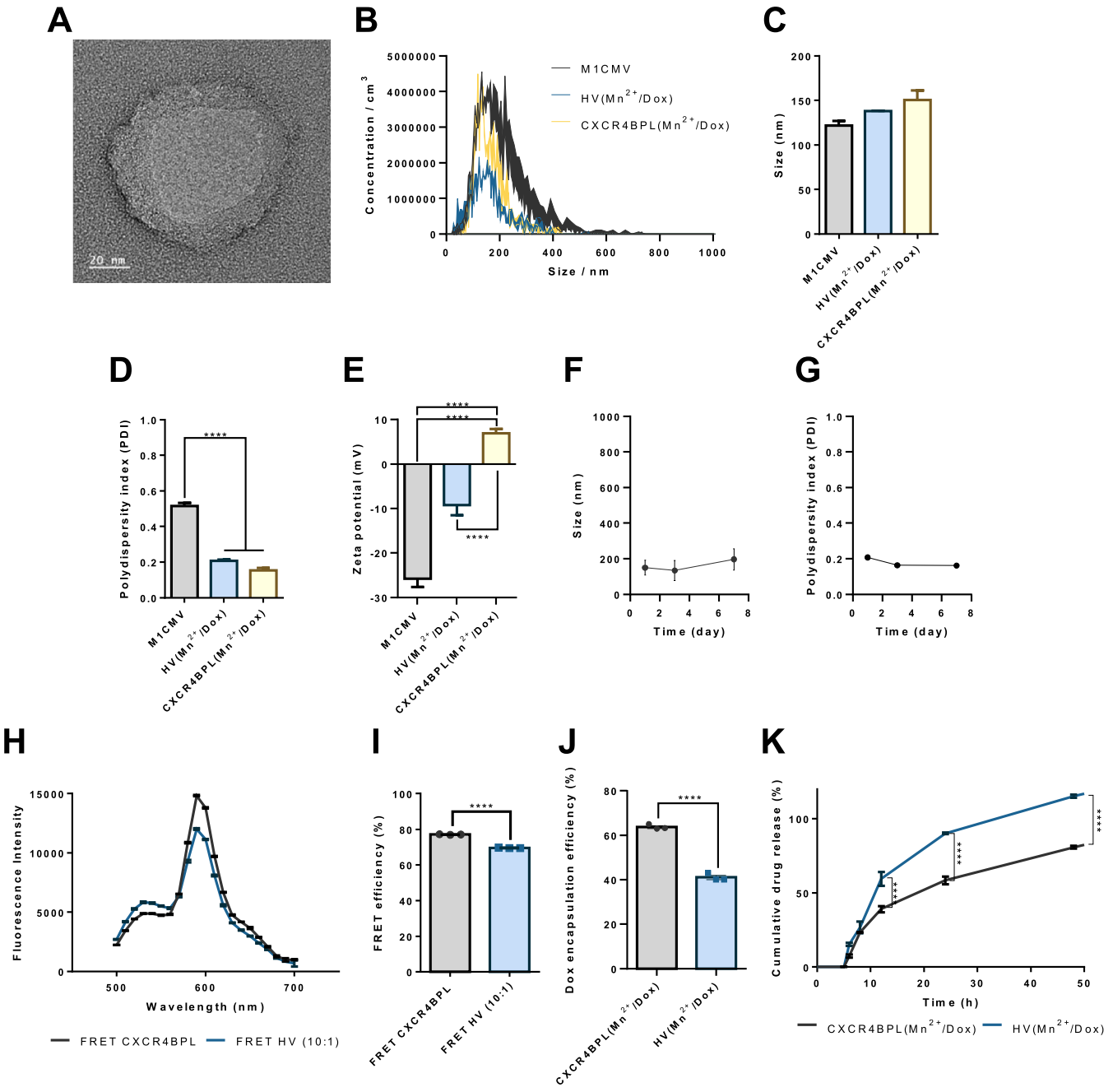

Figure 3. Characterization of M1CMV, CXCR4BPL(Mn^{2+}/Dox), and HV(Mn^{2+}/Dox). (A) FE-TEM image of the HV(Mn^{2+}/Dox). Scale bar = 20 nm. (B, C) Size distribution analysis by nanoparticle tracking. (D) Polydispersity index (PDI) and (E) zeta potential analysis by dynamic light scattering. (F, G) Stability testing of HV(Mn^{2+}/Dox) in PBS for 7 days. (H, I) FRET study showing successful hybridization of CXCR4BPL and M1CMV (10:1 molar ratio). (J) Dox encapsulation efficiencies and (K) cumulative release kinetics of Dox from CXCR4BPL(Mn^{2+}/Dox) and HV(Mn^{2+}/Dox). Data represent mean ± SEM; $n = 3$ (C–E, I–K) from biologically independent samples. ****$p < 0.0001$. Data were analyzed using a one-way ANOVA with Tukey's multiple comparison test (C–E), a two-tailed Student's *t*-test (I, J), or a two-way ANOVA with Bonferroni's significant difference post hoc test (K).

with nutritional metal ions.[26−28] As an important intracellular ion, manganese (Mn^{2+}) has been reported to activate cGAS-STING signaling, promote immune cell activation, and serve as an adjuvant to improve the antitumor efficacy of immunotherapy.[26,29] Nonetheless, despite the expanded understanding of metalloimmunotherapy, the development of an innovative biomimetic delivery platform that can mediate combinational therapy between ICD and metal ions is needed urgently.

In this study, we have developed cell-membrane-derived hybrid nanovesicles, HV(Mn^{2+}/Dox), as a new form of systemic cancer immunotherapy (Figure 1). Briefly, to trigger antitumor proinflammatory immune responses and reverse the immunosuppressive TME, we first derived cell membrane vesicles from M1-like macrophages (M1CMV). M1CMV was then fused with liposomes carrying Mn^{2+} and Dox and decorated with C−X−C chemokine receptor type 4 (CXCR4)-binding peptide (CXCR4BPL). In particular, the CXCR4-binding peptide allows for the targeting of CXCR4-expressing tumor cells while minimizing off-target toxicities.[30,31] Hybridization of M1CMV and CXCR4BPL carrying Mn^{2+} and Dox

https://doi.org/10.1021/acsami.3c18569
ACS Appl. Mater. Interfaces 2024, 16, 17129−17144

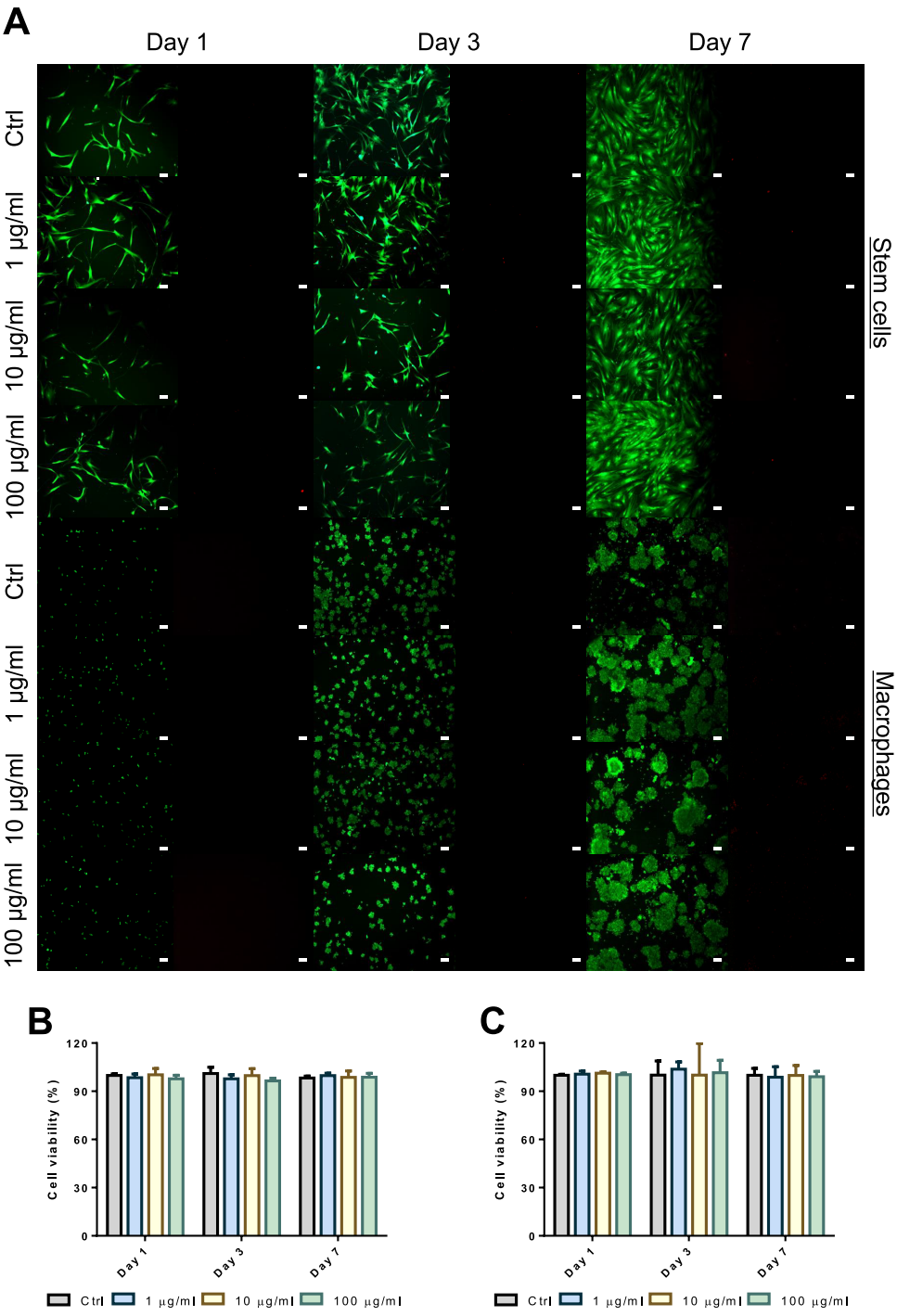

Figure 4. *In vitro* biocompatibility of HV on stem cells and macrophages. (A) Live/dad staining fluorescence microscopy images show hASCs (top panel) and J774A.1 macrophages (bottom panel) incubated with 1, 10, or 100 μg/mL of HV for 1, 3, and 7 days. Live cells were stained with calcein AM (green), while dead cells were stained with ethidium homodimer (EthD-1) (red), all at a magnification of 10×. Scale bar: 50 μm. (B, C) Cell viability of hASCs and J774A.1 macrophages assessed by the CCK-8 assay after 1, 3, or 7 days of incubation with HV (1, 10, and 100 μg/mL), with cell viability normalized to the control (Ctrl). Data represent mean ± SEM; n = 4 (B) and n = 3 (C) from biologically independent samples.

led to the formation of HV(Mn^{2+}/Dox) that exhibits efficient tumor-targeting ability and promotes the delivery of Mn^{2+} and Dox into the TME. Notably, the HV(Mn^{2+}/Dox) treatment triggered M1 macrophage polarization and synergistic proinflammatory immune responses and cytotoxicity *via* codelivery of Mn^{2+}/Dox to CXCR4-expressing tumor cells *in vitro*, and we have shown their potent antitumor efficacy *in vivo*. Overall, the HV(Mn^{2+}/Dox) biomimetic macrophage-derived hybrid vesicle is a promising therapeutic nanoplatform for metalloimmunotherapy in cancer treatment.

RESULTS AND DISCUSSION

Characterizations of M1CMVs, HV(Mn^{2+}/Dox), and CXCR4BPL(Mn^{2+}/Dox). We obtained M1CMVs from J774A.1 macrophage cells treated in M1 polarization

https://doi.org/10.1021/acsami.3c18569
ACS Appl. Mater. Interfaces 2024, 16, 17129−17144

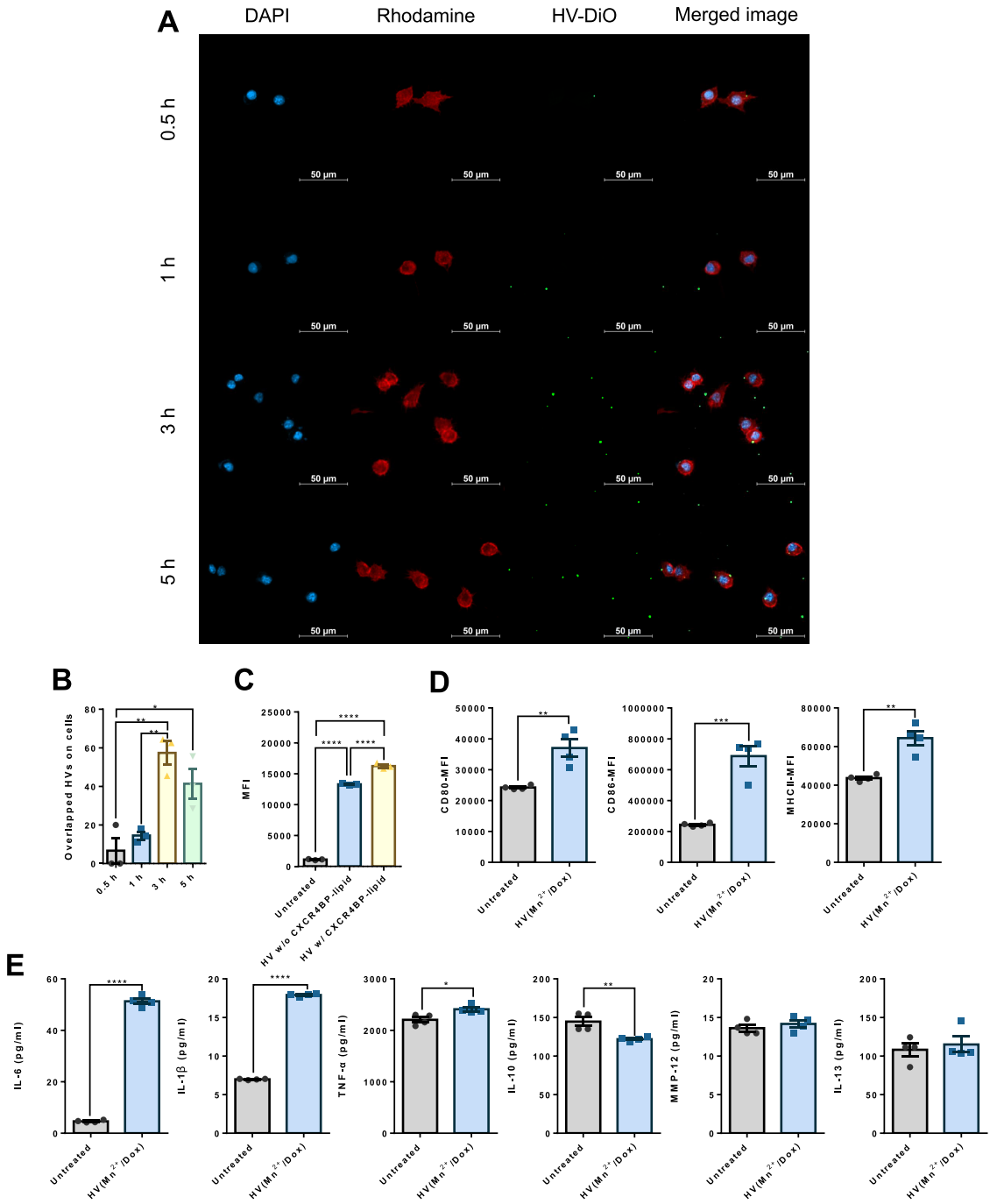

Figure 5. Macrophage-targeting and M1 polarization ability of HV(Mn^{2+}/Dox). (A, B) Confocal microscopy analysis showing the macrophage-targeting ability of HV(Mn^{2+}/Dox) over time. J774A.1 cells were incubated with DiO-labeled HV(Mn^{2+}/Dox) (green) for 0.5, 1, 3, and 5 h. Macrophages were stained with DAPI (blue) and rhodamine-phalloidin (red) to visualize the nucleus and cytoplasm, respectively. Scale bar: 50 μm. (C) Flow cytometry analysis of the cellular uptake of DiO-labeled HV(Mn^{2+}/Dox) with or without CXCR4BP-lipid after 3 h of incubation. (D) Expression levels of surface markers, CD80, CD86, and MHCII, on J774A.1 macrophages after HV(Mn^{2+}/Dox) treatment, as measured by flow cytometry. (E) Concentrations of IL-6, IL-1β, TNF-α, IL-10, MMP-12, and IL-13 secreted by J774A.1 macrophages after HV(Mn^{2+}/Dox) treatment, as determined by ELISA. Data represent mean ± SEM; n = 3 (B, C) and n = 4 (D, E) from biologically independent samples. *p < 0.05, **p < 0.01, ***p < 0.001, ****p < 0.0001. Data were analyzed using a one-way ANOVA with Tukey's multiple comparison test (B, C) or a two-tailed Student's t-test (D, E).

conditions with lipopolysaccharide (LPS) and IFN-γ. J774A.1 macrophage cells were treated *in vitro* with 100 ng/mL of LPS and 50 ng/mL of IFN-γ, followed by enzyme-linked immunosorbent assay (ELISA)-based analysis of the cell culture media after 24, 48, or 72 h of incubation. The ELISA results revealed that J774A.1 macrophage cells treated for 24 h with LPS and IFN-γ produced the highest level of TNF-α with increased levels of IL-6 and reduced levels of the anti-inflammatory cytokine IL-10 (Figure S1), which are functional characteristics of M1-like polarized macrophages. Thus, we produced M1CMVs from J774A.1 cells treated with LPS and

https://doi.org/10.1021/acsami.3c18569
ACS Appl. Mater. Interfaces 2024, 16, 17129−17144

IFN-γ for 24 h. The analysis of the resulting M1CMVs is discussed below.

To synthesize CXCR4BP-lipid, the peptide sequence-KPVSLSYRC, an analog of the stromal-cell-derived factor-1 (SDF-1) peptide sequence,[32−34] was conjugated with maleimide−PEG(2000)−DSPE (yield: 87.5%) *via* the sulfhydryl−maleimide coupling method. The sulfhydryl group (−SH) of the peptide was reacted with the maleimide group on PEG(2000)−DSPE to form a stable thioether bond, resulting in a peptide−lipid conjugate (Figure 2A). Reaction completion was confirmed by the disappearance of the characteristic peak of the maleimide group at 6.8 ppm in the ^{1}H NMR spectrum,[35] indicating successful conjugation of the peptide to the lipid *via* the sulfhydryl−maleimide coupling reaction (Figure 2B,2C). In addition, we confirmed the conjugation of CXCR4-binding peptide to lipids by high-performance liquid chromatography (HPLC) (Figure 2D). After maleimide−PEG(2000)−DSPE was incubated with the CXCR4-binding peptide, the lipid peak at 21.5 min disappeared, indicating that the peptide was successfully linked to the lipid, as seen by the change in retention time compared with the starting materials (Figure 2D). We then inserted CXCR4BP-lipid into liposomes by thin-film hydration method. BCA analysis of the resulting CXCR4BPL indicated the successful incorporation of CXCR4BP-lipid into liposomes in a dose-dependent manner (Figure 2C).

HV(Mn^{2+}/Dox) was obtained by hybridizing M1CMVs with Mn^{2+}/Dox-loaded CXCR4BPL by using probe sonication (Figure 1). Field emission-transmission electron microscopy (FE-TEM), nanoparticle tracking analysis (NTA), and dynamic light scattering (DLS) were used to determine the morphology and size distribution of the particles. The HV(Mn^{2+}/Dox) hybrid vesicles were spherical (Figure 3A) with a diameter of 138.2 ± 0.6 nm (Figure 3C). NTA and DLS analyses further revealed that the hybrid vesicles exhibited a narrow size distribution (polydispersity index: 0.21 ± 0.01) (Figure 3B,D). CXCR4BPL(Mn^{2+}/Dox) displayed a positive zeta potential due to the surface peptide, whereas M1CMV had a negative zeta potential, as it originated from the cell membrane. The hybridization of CXCR4BPL(Mn^{2+}/Dox) with M1CMV led to an increased zeta potential (−9.2 ± 2.3 mV) (Figure 3E), suggesting that HV(Mn^{2+}/Dox) is a hybrid of M1CMV and CXCR4BPL(Mn^{2+}/Dox). The stability of HV(Mn^{2+}/Dox) in PBS was evaluated by measuring the hydrodynamic size and PDI by DLS. As shown in Figure 3F,3G, the physical characterization of HV(Mn^{2+}/Dox) analyzed throughout a 1 week study revealed high stability of HV(Mn^{2+}/Dox) without any major changes in their particle size or PDI values. To confirm hybridization between CXCR4BPL and M1CMV, a Förster resonance energy-transfer (FRET) assay was performed, which has been widely used to study membrane fusion.[20,36] The FRET efficiency before and after the hybridization of CXCR4BPL and M1CMV was monitored (Figure 3H,I). We observed a 7.5% decrease in the FRET efficiency after hybridization due to the decreased distance between the FRET pair (Figure 3I), which indicated the successful insertion of M1CMV into the lipid bilayer of CXCR4BPL.

Next, we examined the drug-loading and release kinetics from CXCR4BPL and HV. Dox was loaded into CXCR4BPL using a modified pH-gradient loading method,[37] resulting in a >60% encapsulation efficiency in CXCR4BPL (Figure 3J) and maintenance of a 40% encapsulation efficiency after hybridization with M1CMV into HV(Mn^{2+}/Dox). Mn^{2+} was also efficiently loaded into HV(Mn^{2+}/Dox) with a loading capacity of 667 ng/10^9 hybrid vesicles. A Dox release study was performed to investigate the release kinetics at normal physiological pH (pH 7.4, PBS) (Figure 3K). Both CXCR4BPL(Mn^{2+}/Dox) and HV(Mn^{2+}/Dox) showed a sustained release of Dox with a relatively higher level of release from HV(Mn^{2+}/Dox) than that from CXCR4BPL-(Mn^{2+}/Dox). We speculate that the higher release profile at later time points for HV(Mn^{2+}/Dox) is due to the lower cholesterol content within the surface, compared with CXCR4BPL(Mn^{2+}/Dox).

***In Vitro* Biocompatibility of HV Treatment on Stem Cells and Macrophages.** Biocompatibility of therapeutic agents is a critical factor influencing their applicability in clinical settings. To assess the biocompatibility of HV, human adipose-derived stem cells (hASCs) and J774A.1 macrophages were incubated with increasing concentrations of HV (1, 10, and 100 μg/mL) for 7 days and monitored for cytotoxicity with a live/dead cell assay, followed by fluorescence microscopy. As shown in Figure 4A, hASCs and J774A.1 macrophages treated with various concentrations (1, 10, and 100 μg/mL) of HV particles remained viable without any significant cytotoxicity. The quantitative cell viability was further confirmed by a CCK-8 assay. As shown in Figure 4B,4C, there was no significant reduction in cell viability at any concentrations of HV tested. These results show that HVs, which emulate a cell membrane, are biocompatible and suitable for *in vivo* applications.

Macrophage-Targeting and M1 Polarization Potentials of HV(Mn^{2+}/Dox). The targeting capability of HV-(Mn^{2+}/Dox) toward specific target immune cell subsets, such as macrophages, is crucial for the improved efficacy of immune-modulating treatments. The macrophage-cell-targeting ability of HV(Mn^{2+}/Dox) was examined using confocal microscopy (Figure 5A,5B). We used murine J774A.1 cells as a representative cell line for macrophages. Figures 5A and S2 show the time-dependent internalization of HV(Mn^{2+}/Dox) by J774A.1 macrophages. The progressive increase in green fluorescence within the cells over 5 h indicated the efficient uptake of HV(Mn^{2+}/Dox) by J774A.1 macrophages. The quantitative analysis in Figure 5B further supported these findings, showing an increase in the percentage of macrophages positive for the DiO-labeled HV signal. Moreover, in order to test whether CXCR4BP-lipid improves targeting and cellular uptake of HV, we examined the cellular uptake of HV modified with or without CXCR4BP-lipid. After 3 h of incubation, we observed a significantly higher cellular uptake of HV(Mn^{2+}/Dox) with CXCR4BP-lipid among J774A.1 cells, compared to HV(Mn^{2+}/Dox) without CXCR4BP-lipid (Figure 5C), suggesting the efficient intracellular delivery of CXCR4-targeted HV(Mn^{2+}/Dox) into macrophage cells known to express high levels of CXCR4.[38,39]

Next, we investigated whether HV(Mn^{2+}/Dox) can polarize naïve J774A.1 cells (representing M0-like macrophages) toward the M1 phenotype. The immunomodulatory effect of HV(Mn^{2+}/Dox) on macrophages was assessed by measuring the expression of surface markers associated with M1 polarization using flow cytometry. As shown in Figure 5D, HV(Mn^{2+}/Dox) treatment increased the expression of CD80, CD86, and MHCII on macrophages, which are indicative markers of M1-like proinflammatory macrophages. Furthermore, M0-like macrophages were incubated with HV(Mn^{2+}/

https://doi.org/10.1021/acsami.3c18569
ACS Appl. Mater. Interfaces 2024, 16, 17129−17144

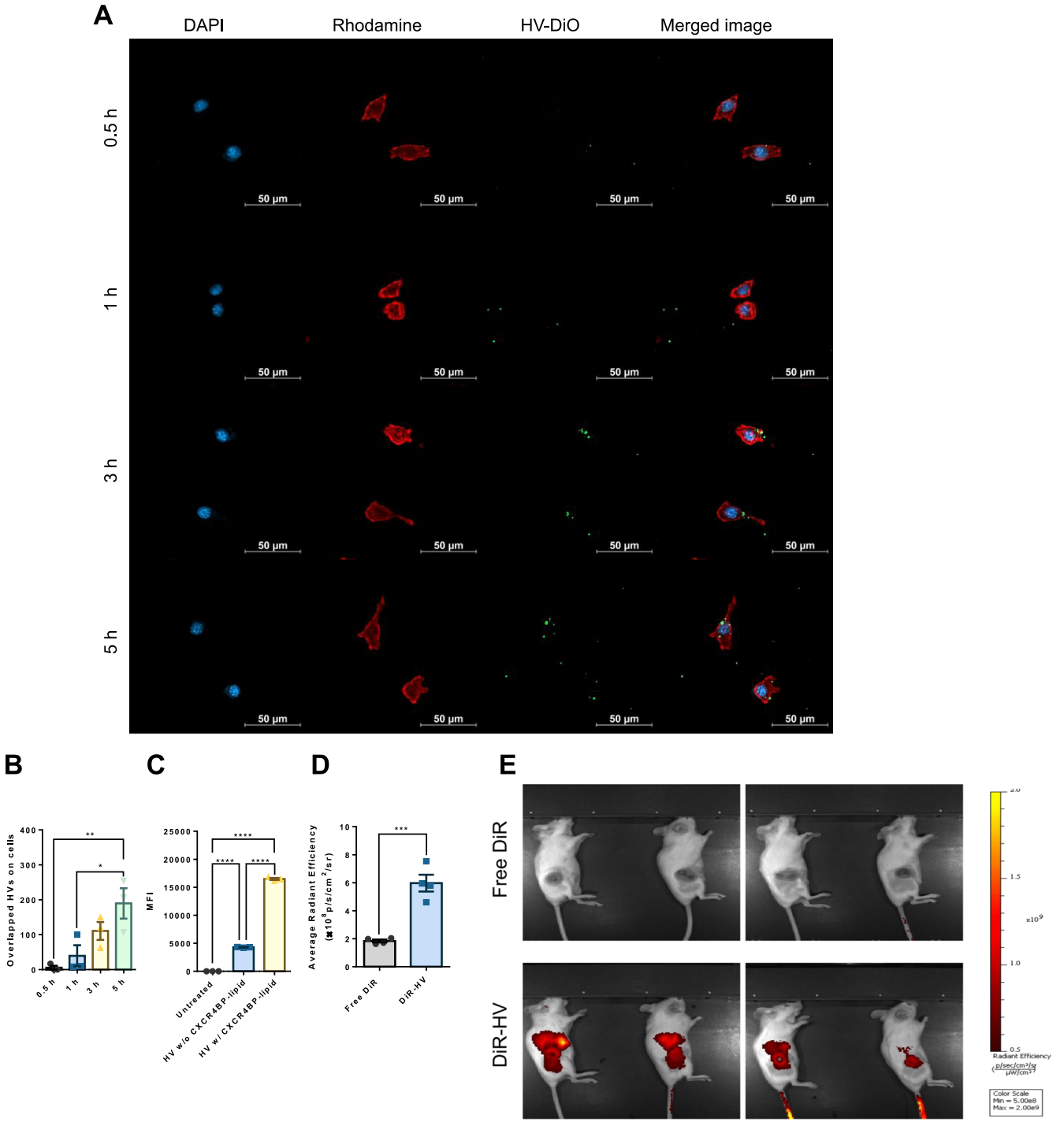

Figure 6. Cancer-targeting efficacy of HV(Mn^{2+}/Dox) *in vitro* and *in vivo*. (A, B) Confocal microscopy analysis shows the intracellular localization of DiO-labeled HV(Mn^{2+}/Dox) (green) in CT26 cells after 0.5, 1, 3, or 5 h of treatment. CT26 cells were stained with DAPI (blue) and rhodamine-phalloidin (red) to visualize the nucleus and cytoplasm, respectively. Scale bar: 50 μm. (C) Flow cytometry analysis of the cellular uptake of DiO-labeled HV(Mn^{2+}/Dox) with or without CXCR4BP-lipid after 3 h of incubation. (D, E) *In vivo* biodistribution analysis of free DiR and DiR-labeled HV(Mn^{2+}/Dox) in 4T1 tumor-bearing mice at 24 h post intravenous injection. Data represent mean ± SEM; $n = 3$ (B, C) and $n = 4$ (D) from biologically independent samples. *$p < 0.05$, **$p < 0.01$, ***$p < 0.001$, ****$p < 0.0001$. Data were analyzed using a one-way ANOVA with Tukey's multiple comparison test (B, C) and a two-tailed Student's *t*-test (D).

Dox) for 24 h, followed by ELISA-based analysis of the supernatant for IL-6, IL-1β, TNF-α, IL-10, MMP-12, and IL-13, the cytokines associated with the M1 and M2 markers, respectively (Figure 5E). Compared with the untreated group, HV(Mn^{2+}/Dox) treatment significantly increased the levels of proinflammatory cytokines IL-6 ($p < 0.0001$), IL-1β ($p < 0.0001$), and TNF-α ($p < 0.05$), which are cytokines associated with M1-like proinflammatory macrophages. As for cytokines and factors associated with M2-like anti-inflammatory macrophages, IL-10 ($p < 0.01$) was decreased, while the levels of MMP-12 and IL-13 were not changed after HV(Mn^{2+}/Dox) treatment. Together, these results suggest that HV(Mn^{2+}/Dox)

https://doi.org/10.1021/acsami.3c18569
ACS Appl. Mater. Interfaces 2024, 16, 17129−17144

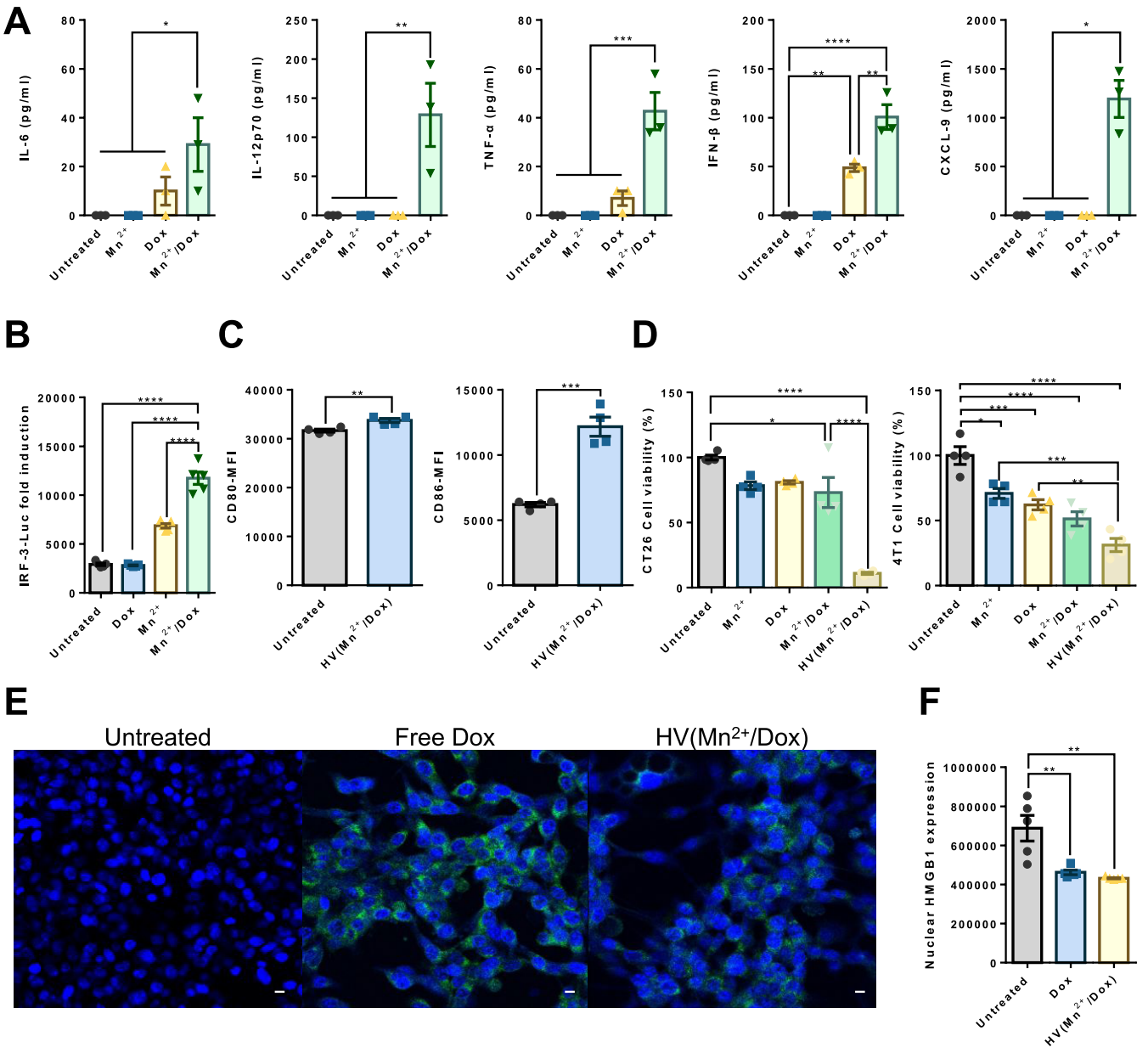

Figure 7. Synergistic effects of Mn^{2+}/Dox and anticancer efficacy of HV(Mn^{2+}/Dox). (A) Mn^{2+}/Dox combination effect on dendritic cell activation. (B) Mn^{2+}/Dox combination effect on the activation of the STING pathway as detected by the THP-1 STING-IRF3 induction reporter cell line. (C) *In vitro* BMDC activation by HV(Mn^{2+}/Dox) treatment for 18 h, with flow cytometry analysis. (D) *In vitro* cytotoxicity induced by HV(Mn^{2+}/Dox) in CT26 or 4T1 cancer cells. (E) Immunogenic cell death (ICD) biomarker analysis through CRT (calreticulin) expression, indicative of ICD. Scale bar: 10 μm. (F) ICD biomarker analysis showing the quantification of HMGB1 nuclear content. Data represent mean ± SEM; $n = 3$ (A), $n = 4$ (C, D), and $n = 5$ (B, F) from biologically independent samples. *$p < 0.05$, **$p < 0.01$, ***$p < 0.001$, ****$p < 0.0001$. Data were analyzed using a one-way ANOVA with Tukey's multiple comparison test (A, B, D, F) and a two-tailed Student's *t*-test (C).

exhibited a macrophage-targeting capacity and induced polarization of M0 macrophages toward the M1 phenotype, which is known to produce proinflammatory cytokines and promote antitumor immune responses.[40]

Cancer-Targeting Efficacy of HV(Mn^{2+}/Dox). Cancer-cell-targeted delivery of a therapeutic nanocarrier is important for improving the therapeutic efficacy with minimal toxicity. We examined the cancer-cell-targeting ability of HV(Mn^{2+}/Dox) using a murine cancer cell line. Murine CT26 and 4T1 cells were used as representative colon adenocarcinoma and breast cancer cell lines, respectively, for the study. Both CT26 and 4T1 cells expressed CXCR4 (Figure S3). *In vitro* confocal microscopy analysis demonstrated the cellular internalization of HV(Mn^{2+}/Dox) into the cytoplasm of CT26 cells over time (Figure 6A,B), showing efficient intracellular delivery of HV into cancer cells. Figures 6A and S4 revealed a time-dependent internalization of DiO-labeled HV(Mn^{2+}/Dox) by CT26 cancer cells, with a substantial increase in intracellular green DiO fluorescence observed over a 5 h period. Quantitative analysis confirmed the visual observation, demonstrating an increase in the percentage of cancer cells with DiO-labeled HV(Mn^{2+}/Dox) uptake over time (Figure 6B). This indicates the successful and efficient uptake of HV(Mn^{2+}/Dox) by tumor cells. To substantiate these findings further with quantitative analysis, a flow cytometry assay using the CT26 cells was performed. Figure 6C shows the flow cytometry

https://doi.org/10.1021/acsami.3c18569
ACS Appl. Mater. Interfaces 2024, 16, 17129−17144

analysis of DiO-labeled HV(Mn^{2+}/Dox) without CXCR4BP-lipid or HV(Mn^{2+}/Dox) with CXCR4BP-lipid after 3 h of treatment. CT26 cells displayed significantly higher uptake of HV(Mn^{2+}/Dox) with CXCR4BP-lipid than HV(Mn^{2+}/Dox) without CXCR4BP-lipid ($p < 0.0001$), suggesting efficient targeting and internalization of HV(Mn^{2+}/Dox) modified with CXCR4BP-lipid into CXCR4-expressing cancer cells.[41] HV-(Mn^{2+}/Dox) also showed higher cellular uptake to 4T1 cells (Figure S5), demonstrating the cancer-targeting ability by CXCR4BP-lipid on HV(Mn^{2+}/Dox). Therefore, both confocal imaging and flow-cytometry-based quantitative analysis provided compelling evidence of effective targeting of HV(Mn^{2+}/Dox) to CXCR4-expressing cancer cells *in vitro*.

To validate the *in vitro* findings, we extended our investigation to an *in vivo* model. 4T1 tumor-bearing mice were administered with either free DiR or DiR-labeled HV(Mn^{2+}/Dox) to track the biodistribution of HV(Mn^{2+}/Dox). *In vivo* imaging studies (Figure 6E) showed minimal accumulation of free DiR in the 4T1 tumor region, suggesting rapid clearance or nonspecific distribution. In contrast, the DiR-labeled HV(Mn^{2+}/Dox) group showed a pronounced fluorescence signal in the 4T1 tumor site, indicating the tumor-targeted delivery of HV(Mn^{2+}/Dox). The average pixel intensity analysis further corroborated these findings, with a marked increase in the fluorescence signal of DiR-labeled HV(Mn^{2+}/Dox) in tumor tissues (Figure 6D).

The collective data from the *in vitro* and *in vivo* analyses provide compelling evidence for the cancer-targeting ability of HV(Mn^{2+}/Dox). The rapid uptake of HV(Mn^{2+}/Dox) by cancer cells *in vitro* and its preferential accumulation at the tumor site *in vivo* highlight the potential of HV(Mn^{2+}/Dox) as a drug delivery system in cancer therapy. The specificity of HV(Mn^{2+}/Dox) for cancer cells could allow for an increased drug concentration at the target site, potentially enhancing treatment efficacy while minimizing systemic toxicity.

Synergistic Immune Stimulation by Mn^{2+}/Dox and *In Vitro* Anticancer Efficacy of HV(Mn^{2+}/Dox). Harnessing the power of the immune system is pivotal in the fight against cancer. The combination of Mn^{2+} and Dox exploits their potential synergistic effects on immune activation. The combination effect of Mn^{2+} and Dox on immune activation was examined *in vitro* by evaluating the levels of dendritic cell (DC) activation based on the cytokine release profiles indicative of immune stimulation. Cotreatment of Mn^{2+} and Dox significantly upregulated the production of proinflammatory cytokines and chemokines (IL-6 ($p < 0.05$), IL-12p70 ($p < 0.01$), TNF-α ($p < 0.001$), IFN-β ($p < 0.0001$), and CXCL-9 ($p < 0.05$)) in DCs (Figure 7A) compared to untreated controls, Mn^{2+} alone, and Dox alone, showcasing that the combination of dual agents effectively promoted DC maturation. The STING pathway plays a crucial role in the innate immune response to tumors. We have previously reported that Mn^{2+} can potentiate the STING pathway to produce type-I interferon cytokines, leading to enhanced cancer immunotherapy efficacy.[26] We utilized a STING-IRF3 induction reporter cell line derived from THP-1 cells (a human monocytic cell line) to investigate the activation of the cGAS/STING pathway. While Mn^{2+} individually induced an increase in IRF3 activation above the untreated control, the combination of Dox and Mn^{2+} resulted in a 4-fold induction markedly higher than that observed with either agent alone (Figure 7B). This heightened response indicates a synergistic effect of Mn^{2+} and Dox in promoting the cGAS/STING pathway, which is a central mediator of the innate immune response against cancerous cells. The data reveal that the combination of Mn^{2+} and Dox elevates the IRF3 induction level to a degree that suggests the potent stimulation of the cGAS/STING pathway. This analysis directly demonstrates the engagement of the cGAS/STING pathway following treatment, supporting the hypothesis that a combination of Mn^{2+} and Dox can indeed trigger an innate immune response conducive to cancer immunotherapy. The proposed mechanism involves the Mn^{2+}-mediated activation of cGAS, leading to increased production of cyclic GMP−AMP (cGAMP), the secondary messenger that activates STING. Activated STING then leads to the transcriptional upregulation of IRF3, culminating in the production of type-I interferons and other cytokines that can enhance the antitumor immune response. This phenomenon elucidates the underlying cause of the observed potentiation of the immune response, which is critical for the development of more effective cancer immunotherapies.

We further investigated the direct impact of HV(Mn^{2+}/Dox) on bone marrow-derived dendritic cells (BMDCs) *in vitro*. Following 18 h of treatment with HV(Mn^{2+}/Dox), flow cytometry analysis revealed a marked increase in the expression of costimulatory molecules, CD80 and CD86 (Figure 7C), confirming the activation of BMDCs by HV(Mn^{2+}/Dox). This activation is a preliminary step toward initiating a robust antitumor T cell response.

Based on our previous findings, we hypothesized that the codelivery of Mn^{2+} and Dox *via* HV(Mn^{2+}/Dox) would improve cancer immunotherapy by reshaping the tumor microenvironment and triggering anticancer immunity. First, the cancer cell killing capacity of HV(Mn^{2+}/Dox) was evaluated *in vitro* using CT26 and 4T1 cancer cells. HV(Mn^{2+}/Dox) treatment notably enhanced the cytotoxicity, compared with soluble Mn^{2+} alone, Dox alone, or their combination (Figure 7D). In fact, HV(Mn^{2+}/Dox) achieved approximately 62 and 20% higher cytotoxic efficiencies than Mn^{2+}/Dox after 24 h of treatment in CT26 and 4T1, respectively. This enhanced killing by HV(Mn^{2+}/Dox) can be attributed to HV-mediated intracellular delivery of Mn^{2+} and Dox into the cytoplasm of cancer cells through interaction between HV and the cellular membrane. This is notable as the efficient intracellular uptake of bioactive cargo is crucial for eliciting robust cytotoxicity.[42]

The rationale behind the combinatorial effect of Mn^{2+} and Dox lies in their ability to effectively induce immunogenic cell death and DNA damage, activate the cGAS/STING pathway, and enable macrophages and dendritic cells to enhance the presentation of cancer antigens, thus intensifying tumor-specific adaptive immunity.[43,44] The induction of immunogenic cell death (ICD) is a desirable effect of anticancer therapies, as it can enhance the immune system's ability to recognize and eliminate cancer cells. The expression of the ICD biomarker calreticulin (CRT) on the cell surface was increased after HV(Mn^{2+}/Dox) treatment (Figure 7E), indicating the initiation of ICD.[45,46] Additionally, the quantification of HMGB1 in the nuclei of cancer cells revealed a decrease in nuclear HMGB1 after treatment with HV(Mn^{2+}/Dox) (Figure 7F), further supporting the induction of ICD by the HV(Mn^{2+}/Dox).

These *in vitro* studies collectively highlight the dual functionality of HV(Mn^{2+}/Dox). By activating DCs through the synergistic effects of Mn^{2+} and Dox and demonstrating

https://doi.org/10.1021/acsami.3c18569
ACS Appl. Mater. Interfaces 2024, 16, 17129−17144

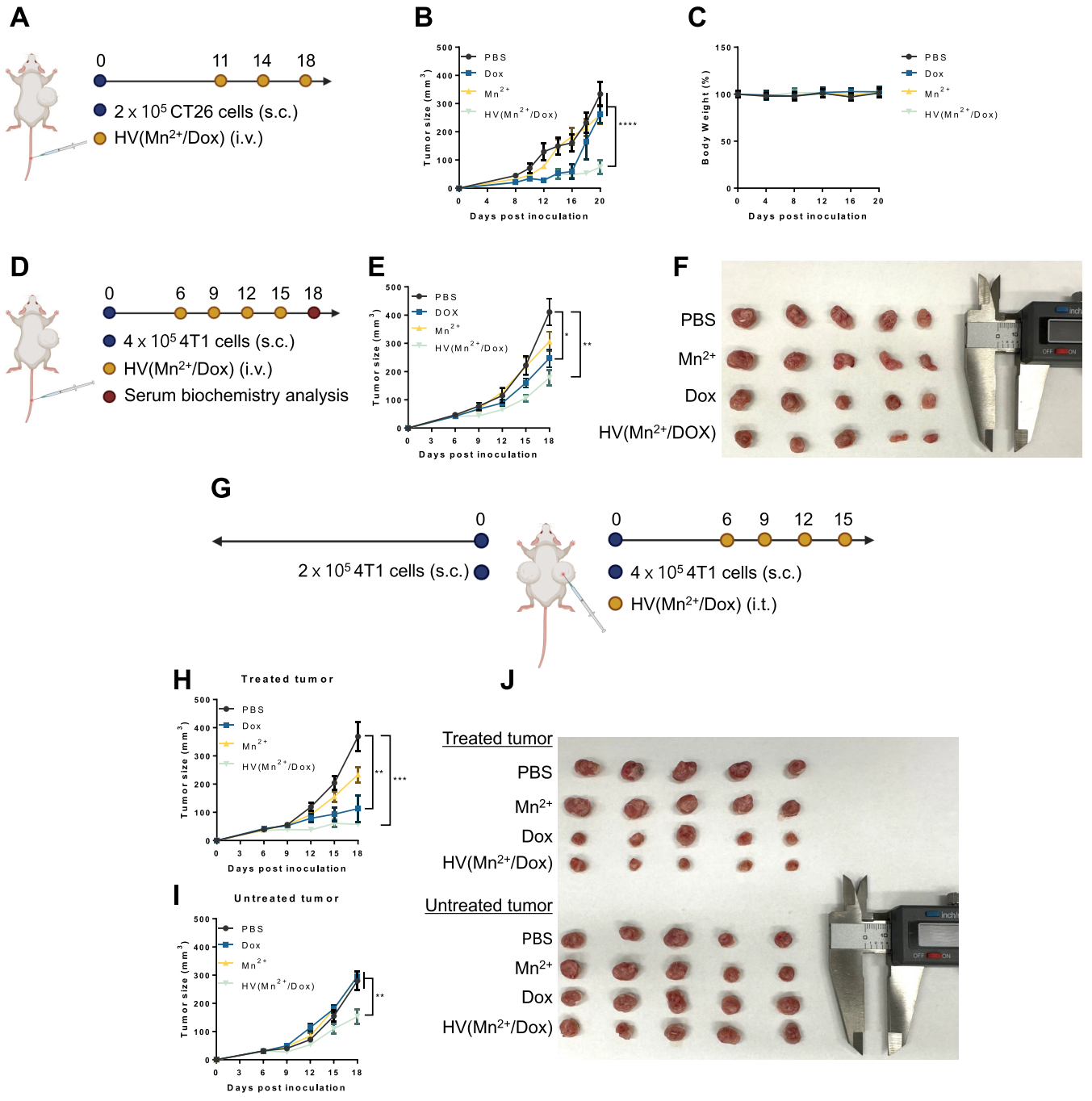

Figure 8. *In vivo* anticancer efficacy of HV(Mn^{2+}/Dox). (A–C) BALB/c mice were inoculated s.c. with 2×10^5 CT26 cells, and on days 11, 14, and 18, mice were treated by intravenous (i.v.) administration of PBS, Dox (2 mg/kg), Mn^{2+}, or HV(Mn^{2+}/Dox) (2 mg/kg Dox equiv). Panel (B) shows the tumor volume and (C) body weight changes over time. (D–F) BALB/c mice were inoculated s.c. with 4×10^5 4T1 cells, and on days 6, 9, 12, and 15, mice were treated by i.v. administration of PBS, Dox (2 mg/kg), Mn^{2+}, or HV(Mn^{2+}/Dox) (2 mg/kg Dox equiv). Panel (C) shows the tumor volume and (D) representative images of excised tumors on day 18. (G–J) BALB/c mice were inoculated s.c. with 4×10^5 4T1 cells on the right and 2×10^5 4T1 cells on the left flank, and on days 6, 9, 12, and 15, only the right flank tumor treated by intratumoral administration of PBS, Dox (2 mg/kg), Mn^{2+}, or HV(Mn^{2+}/Dox) (2 mg/kg Dox equiv). Panel (E) shows the volume of the treated tumor, (F) volume of untreated, contralateral tumor, and (G) representative images of excised tumors on day 18. Data represent mean ± SEM; $n = 4$ (A, B), and $n = 5$ (C, E, F) from biologically independent samples. $^*p < 0.05$, $^{**}p < 0.01$, $^{***}p < 0.001$, $^{****}p < 0.0001$. Data were analyzed using a two-way ANOVA with Tukey's multiple comparison test (A–C, E, F).

direct cytotoxicity toward cancer cells, HV(Mn^{2+}/Dox) emerges as a promising candidate for cancer immunotherapy. Its ability to stimulate the immune system and directly target tumor cells may provide a multipronged approach to combating cancer, potentially enhancing treatment efficacy while minimizing systemic toxicity.

***In Vivo* Anticancer Efficacy of HV(Mn^{2+}/Dox).** We hypothesized that HV-mediated codelivery of Mn^{2+}/Dox and M1 polarization of macrophages could activate both innate and adaptive immunities, thus promoting anticancer activities by converting "cold tumors" to "hot tumors". For the proof-of-concept studies, *in vivo* anticancer efficacy of HV(Mn^{2+}/Dox)

https://doi.org/10.1021/acsami.3c18569
ACS Appl. Mater. Interfaces 2024, 16, 17129–17144

was evaluated in the CT26 and 4T1 syngeneic tumor models. In single tumor models (Figure 8A−8C), we intravenously administered free Dox (2 mg/kg), free Mn^{2+}, or HV(Mn^{2+}/Dox) (equivalent dose as free Dox) to mice-bearing CT26 tumor. Tumor volume measurements over time revealed that HV(Mn^{2+}/Dox) inhibited tumor growth (77.6 ± 7.1%) compared to the untreated group in the CT26 model (Figure 8B). The mean body weights of both treatment groups were comparable to those of the untreated control group (Figure 8C). The free Dox group displayed minimal changes in body weight after the initial injection, which is attributed to the small dosage used, which is in line with the amount of Dox present in HV(Mn^{2+}/Dox) formulation. The low dosage of the free Dox treatment failed to induce significant inhibitory effects on tumor growth, as depicted in Figure 8B, which highlights its limited efficacy. In contrast, the HV(Mn^{2+}/Dox) treatment group showed higher anticancer efficacy despite the low dosage of Dox. Remarkably, HV(Mn^{2+}/Dox) achieved this effect without inducing any discernible systemic toxicities. Moreover, we have validated these results using the 4T1 tumor model. Similar to the CT26 tumor model, HV(Mn^{2+}/Dox) therapy led to strong suppression of 4T1 tumor growth in 4T1 tumor-bearing mice (Figure 8D−F). Additionally, the serum biochemical analyses of 4T1 tumor-bearing mice treated with either PBS or HV(Mn^{2+}/Dox) showed no significant signs of toxicity (Figure S6).

We also examined the systemic antitumor efficacy of local HV(Mn^{2+}/Dox) treatment using a bilateral 4T1 tumor model (Figure 8G,8J). This bilateral model allows for the direct assessment of treated local tumors as well as systemic abscopal effects on distant, untreated tumors. Anticancer efficacy evaluation in the 4T1 bilateral tumor model indicated that local intratumoral treatment with HV(Mn^{2+}/Dox) exerted robust antitumor activity on the treated local tumors (Figure 8H), and this also led to significantly suppressed tumor growth in untreated, contralateral tumors ($p < 0.01$) (Figure 8I). The excised tumors from the bilateral 4T1 model showed reduced tumor size in both treated and untreated sites (Figure 8J). These data collectively suggest that HV(Mn^{2+}/Dox) not only exhibits strong anticancer properties at the site of administration but may also stimulate systemic antitumor immune responses, potentially leading to the regression of untreated tumors.

These results pointed to the perspective that our HV(Mn^{2+}/Dox) strategy could concentrate cytotoxicity on cancer cells while preventing toxicities in normal cells by CXCR4BP-mediated-enhanced tumor targeting. The targeted delivery of HV(Mn^{2+}/Dox) to the tumor site contributes to the transformation of the tumor microenvironment by increasing the M1 macrophage polarization and activating DCs, thereby improving therapeutic efficacy. These results also support the synergistic effect of combining Mn^{2+} and Dox in augmenting anticancer activities, evidenced by sustained tumor suppression even with a low dosage of HV(Mn^{2+}/Dox).

CONCLUSIONS

In summary, we designed Mn^{2+}/Dox-loaded hybrid vesicles (HV(Mn^{2+}/Dox)) composed of M1CMV and CXCR4BPL for enhanced anticancer efficacy. *In vitro* experiments showed that HV(Mn^{2+}/Dox) enables the delivery of dual functionality. Additionally, the dual Mn^{2+}/Dox treatment demonstrates the ability to promote anticancer agents (Mn^{2+}/Dox), along with M0-to-M1 reprogramming. The HVs specifically polarized macrophages toward the M1 phenotype, thereby increasing proinflammatory cytokine levels. The HVs exhibited favorable macrophage- and tumor-targeting capacities, ascribed to the CXCR4-binding peptide, which promoted attachment to cancer cells, higher M1 polarization, and DC maturation, leading to tumor growth inhibition. Both *in vitro* and *in vivo* experiments have proved that HV(Mn^{2+}/Dox) has satisfactory inhibitory effects on antitumor efficacy. Overall, HV(Mn^{2+}/Dox) showed favorable results with strong antitumor therapeutic effects, making it a promising multi-anti-cancer-agent delivery system for cancer immunotherapy and chemotherapeutics.

EXPERIMENTAL METHODS

Cell Culture. J774A.1 murine macrophage cells and human adipose-derived stem cells (hASCs) were cultured in Dulbecco's modified Eagle's medium (DMEM). CT26 colon carcinoma cells were cultured at Roswell Park Memorial Institute (RPMI)-1640. Cell lines were incubated at 37 °C in a 5% CO_2-humidified atmosphere. All cell culture media included 1% (v/v) penicillin/streptomycin and 10% (v/v) fetal bovine serum (FBS).

***In Vitro* Macrophage Polarization.** M1-polarized macrophages were induced by culturing the J774A.1 macrophage cell line in DMEM cell culture media with 50 ng/mL of IFN-γ (Sigma-Aldrich) and 100 ng/mL of lipopolysaccharide (LPS) (Sigma-Aldrich) for 24 h. M0-polarized macrophages, induced with phosphate-buffered saline (PBS) for 24 h, were used as the control group. To show that the cells were properly polarized, typical M1/M2-defining cytokines (TNF-α, IL-6, and IL-10) were analyzed using ELISA kits.

Preparation and Characterization of Peptide-Conjugated Lipid. CXCR4-binding peptides (containing an additional cysteine in the N-termini) were conjugated with maleimide−PEG(2000)−DSPE *via* the sulfhydryl−maleimide coupling method.[47] In brief, maleimide−PEG(2000)−DSPE was diluted in chloroform, rotary-evaporated at 37 °C and 120 rpm to form a thin film, and hydrated with pure water at 37 °C. Peptides were dissolved in 0.1 M PBS and mixed with maleimide−PEG(2000)−DSPE (peptides/maleimide−PEG(2000)−DSPE, molar ratio 1.2:1) to react overnight under N_2 gas at room temperature. The mixture was filled in a molecular weight cutoff of a 2 kDa dialysis bag for 48 h to remove the residual free peptides before freeze-drying. The yield was determined by calculating the weight of CXCR4BP-lipid relative to the cumulative mass of the initial components. The ^{1}H NMR spectra and HPLC results were then collected.

Preparation of M1CMV. M1 macrophages were polarized with 100 ng/mL of LPS and 50 ng/mL of IFN-γ for 24 h. About 1×10^7 of LPS/IFN-γ-treated J774A.1 cells (M1 macrophages) were harvested without trypsin and washed twice with ice-cold TM buffer at pH 7.5 (TM buffer, 1× tris-magnesium sulfate, Avantor). The cells were resuspended in 50 mL of TM buffer and incubated for 5 min at 4 °C, then homogenized (IKA T10 basic Homogenizer) at 6 rpm for 5 min, followed by probe sonication. The vesicles were then ultracentrifuged (Beckman Coulter Centrifuge) for 1 h at 150,000 g at 4 °C. The pellets were stored at 4 °C.

Preparation of HV(Mn^{2+}/Dox). The conventional thin-film hydration method was applied to prepare Mn^{2+}/Dox-loaded liposomes[48,49] composed of DOPC (1,2-dioleoyl-*sn*-glycero-3-phosphocholine), cholesterol, and CXCR4BP-lipid (63:27:10, molar ratio). Briefly, the lipids were dissolved in chloroform and the organic solvent was evaporated under reduced pressure at 45 °C with a rotary evaporator to form a thin film. The thin film was hydrated with 300 mM manganese(II) acetate tetrahydrate at 60 °C for 1 h and adjusted to pH 3.5 by the addition of 1 N hydrochloric acid. Following hydration, the multilamellar vesicles (MLVs) were passed through a PD-10 Desalting Column (Cytiva) pre-equilibrated with PBS buffer (pH 7.5) to remove unencapsulated ions. The predissolved Dox was then slowly dropped over the manganese-containing liposomes at 60 °C and stirred for 1 h, such that the final Dox-to-liposomal-lipid ratio

https://doi.org/10.1021/acsami.3c18569
ACS Appl. Mater. Interfaces 2024, 16, 17129−17144

was 0.2 (w/w). The liposomal solution was subjected to sonication in an ice−water bath with M1CMV solutions by probe sonication (on 2 s/off 2 s, 5 min, 26% amplitude). To remove the unencapsulated drugs, the liposomes were again passed through a PD-10 desalting column pre-equilibrated with PBS buffer. The final formulation was stored at 4 °C. DiO-labeled HVs were prepared by the same methods as aforementioned, except that DiO was added before the formation of the thin film.

Physicochemical Characterization of HV(Mn^{2+}/Dox). The mean particle sizes and size distributions of M1CMV, HV(Mn^{2+}/Dox), and CXCR4BPL(Mn^{2+}/Dox) were measured by NTA using a NanoSight NS300 (Malvern Instruments Ltd., Worcestershire, U.K.). The PDIs and zeta potentials (surface charges) of M1CMV, HV(Mn^{2+}/Dox), and CXCR4BPL(Mn^{2+}/Dox) were determined by DLS using a Zetasizer Nano ZS system (Malvern Instruments Ltd., Worcestershire, U.K.). The loading of Mn^{2+} in the HV(Mn^{2+}/Dox) was quantified by inductively coupled plasma-mass spectrometry (ICP-MS; PerkinElmer Nexion 2000). The stability of the vesicles was studied by monitoring changes in size and PDI for up to 7 days. The morphology was confirmed by energy-filtered transmission electron microscopy (EF-TEM). Protein quantifications of the CXCR4BPL and liposomes without peptides were done using the BCA assay.

Elucidation of Hybridization. Validation of hybridization of CXCR4BPLs and M1CMVs producing HVs was done by FRET study.[20] To form FRET CXCR4BPL, FRET fluorophore lipids, with NBD serving as an electron donor and Rh−B serving as an electron acceptor, were added to the lipid mixture in a 1:7 molar ratio. For fusion analysis, FRET CXCR4BPL and CMV (10:1 molar ratio) were hybridized by probe sonication. FRET CXCR4BPLs, before and after fusion of CMVs, were analyzed by fluorescence spectroscopy by exciting the samples at 470 nm and determining the emission spectra between 500 and 700 nm. The percentage of FRET efficiency was calculated through the following equation

$$\text{FRET efficiency (\%)} = \left(\frac{F_a}{F_a + F_b}\right) \times 100 \quad (1)$$

where F_a is the emission fluorescence of the acceptor (Rh−B) and F_b is the emission fluorescence of the donor (NBD).

Dox Encapsulation and Release Profiles. The amount of Dox loaded was calculated by measuring the fluorescence intensity (λ_{ex} = 470 nm; λ_{em} = 595 nm). To calculate the amount of Dox in HV, the HV was destroyed with 1 N HCl. Encapsulation efficiency (EE) was then calculated using formula 2

$$\text{drug encapsulation (\%)} = \left(\frac{\text{amount of Dox encapsulated in HV}}{\text{amount of total Dox}}\right) \times 100 \quad (2)$$

To measure its drug release profile, 250 μL of HV(Mn^{2+}/Dox) was dialyzed against 14 mL of the medium in PBS (pH 7.4) with constant shaking (100 rpm) at 37 °C. At various time intervals, 1 mL of the dialysis buffer solution was taken out for measurement and refilled with an equal volume of a new medium. The released Dox amount was estimated by detecting the absorbance value at the fluorescence intensity (λ_{ex} = 470 nm; λ_{em} = 595 nm).

Biocompatibility Assessment. To evaluate the biocompatibility of HV, live and dead cell staining was performed using the Live/Dead Viability/Cytotoxicity Kit for mammalian cells (Invitrogen, Carlsbad, CA) according to the manufacturer's instructions. Briefly, hASCs and J774A.1 macrophages were seeded at a density of 1×10^5 cells/well and 1×10^4 cells/well, respectively, in 12-well plates and allowed to adhere for 24 h. Subsequently, cells were exposed to HV at various concentrations for 1, 3, and 7 days. After incubation, cells were stained with 2 μM calcein AM and 4 μM ethidium homodimer-1 for 30 min at 37 °C in the dark to distinguish live (green fluorescence) and dead (red fluorescence) cells. Fluorescence images were captured by using a fluorescence microscope. The cell viability of hASC and J774A.1 in the presence of HV was quantified using a CCK-8 assay (Dojindo Molecular Technologies, Inc., Kumamoto, Japan) following the manufacturer's protocol. Cells were seeded in 96-well plates at a density of 1×10^4 cells/well and 1×10^3 cells/well, respectively, and allowed to adhere overnight. HV was then added to the wells in varying concentrations, and the cells were incubated for 1, 3, and 7 days. After incubation, 10% CCK-8 solution was added to each well, and the plates were incubated for an additional 2 h at 37 °C. The absorbance at 450 nm was measured using a microplate reader to determine cell viability. The cell viability was calculated relative to the untreated control wells. The Chung-Ang University Hospital Institutional Review Board approved the use of hASCs, and it was carried out in accordance with the Declaration of Helsinki's criteria (IRB No. 2151−005−463).

***In Vitro* Cellular Uptake of HV(Mn^{2+}/Dox) for Validation of Macrophage and Cancer-Cell-Targeting Ability by Flow Cytometry.** J774A.1 and CT26 cells were treated with a given concentration of DiO-labeled HV without or with CXCR4BP-lipid (1.5×10^{10} particles/ml), and the accumulation of them in the cells was analyzed using a FACS Calibur (Becton Dickinson BD). Cells cultured in the absence of the nanoplatforms were used as the control. The cells (2×10^5 cells/ml) were cultured overnight at 37 °C under a 5% CO_2 atmosphere. Next, the cellular uptakes of DiO-labeled M1CMV and DiO-labeled HV were measured by incubating the cells with 1.5×10^{10} DiO-labeled M1CMV and DiO-labeled HV in RPMI-1640 cell culture medium for CT26 and DMEM cell culture medium for J774A.1 for 3 h. Then, the cells were washed twice with PBS, and the fluorescence was analyzed with flow cytometry. The experiments were repeated at least 3 times.

Macrophage and Cancer Cell Targeting by Confocal Laser Scanning Microscopy (CLSM). J774A.1 and CT26 cells were seeded (2×10^4 cells/chamber) 24 h prior to treatment on four-well glass-chamber slides (SPL, Cell Culture Slide) in the cell culture medium. The cells were treated with fresh medium containing 1.5×10^{10} DiO-labeled HV for 0.5, 1, 3, and 5 h at 37 °C. Following the incubation period, the chambers were washed at least 4 times with PBS (pH 7.4). The cells were incubated in DPBS in the presence of rhodamine-phalloidin for 2 h for cytoplasm staining and in DAPI for 3 min for nuclear staining. The cells were then washed several times with PBS. The chambers were mounted and examined on a Zeiss LSM 900 microscope. ZEISS ZEN lite software was used for the setup, and ImageJ software was used for image processing. The overlapped HVs on cells were calculated using formula 3 and ImageJ software

$$\text{overlapped HVs on cells} = \frac{\text{the number of HVs}}{\text{the number of cells}} \quad (3)$$

Synergistic Effects of Mn^{2+} and Dox. Mouse bone marrow-derived dendritic cells (BMDCs) were prepared according to the literature.[50] BMDCs were seeded (4×10^4 cells/well) in a 96-well round-bottom plate and incubated for 12 h with Dox (10 μg/mL), Mn^{2+} (0.04 μg/mL), or Dox combined with Mn^{2+}. Supernatants were then collected for cytokine analysis by enzyme-linked immunosorbent assay (ELISA; R&D System), including IL-6, IL-12p70, TNF-α, IFN-β, and CXCL-9. To assess the activation of the STING pathway, THP-1 cells stably transfected with an IRF3-responsive luciferase reporter (THP-1-luc-reporter cells, Invivogen) were utilized. Cells were treated with free Dox (1 μM), Mn^{2+} (500 μM), or a combination of free Dox and Mn^{2+}. Post-treatment, cells were incubated for 24 h to allow for pathway activation and subsequent reporter gene expression. Luciferase activity was quantified as a measure of STING pathway activation. The assay was performed using a standard luciferase substrate, and the luminescence intensity was measured on a plate reader. Results were expressed as fold induction over untreated control cells to normalize for baseline activity.

***In Vitro* Analysis of BMDC Activation and Macrophage Polarization by HV Treatment.** For activation assays, BMDCs were seeded and treated with HV (8×10^4 particles/ml) for 18 h. Following incubation, the cells were stained for surface markers CD80, CD86, and MHCII to assess the activation status. Staining was

https://doi.org/10.1021/acsami.3c18569
ACS Appl. Mater. Interfaces 2024, 16, 17129−17144

performed using the following fluorochrome-conjugated antibodies: CD80 (BUV496), CD86 (APC), and MHCII (BV510). Additionally, cells were stained with F4/80 (PE-Cy7) to identify macrophages and a live/dead marker (NIR) to assess cell viability by flow cytometry (Cytek Aurora System). ELISA was performed to determine M1- or M2-type released cytokines (IL-6, IL-1β, TNF-α, IL-10, MMP-12, and IL-13) in the M0 macrophages. M0 J774A.1 macrophages were seeded (1×10^5 cells/well) in 6-well plates and incubated for 24 h, to which HV (1×10^{11} particles/ml) was added. Cells cultured in the absence of the nanoplatforms were used as the control. Supernatants were harvested after 24 h and subjected to ELISA (IL-6, IL-1β, TNF-α, IL-10, MMP-12, and IL-13).

ICD Biomarker Analysis in Cancer Cells. CT26 cells were plated and treated with 1 μM free Dox or an equivalent concentration of Dox in HV(Mn^{2+}/Dox) for 24 h. Post-treatment, the cells were stained for Calreticulin using an anti-Calreticulin antibody (Abcam, ab196158) at a 1:200 dilution. Nuclei were counterstained with Hoechst 33342 (Invitrogen, H3570). CRT expression was visualized by confocal microscopy (Nikon A1). Simultaneously, CT26 cells were also assessed for the nuclear amount of High Mobility Group Box 1 (HMGB1). Cells were treated in the same manner as for CRT expression and subsequently stained with an anti-HMGB1 antibody (Abcam, ab195010) at a dilution of 1:50. Nuclear HMGB1 expression was analyzed using a flow cytometer (Cytek Aurora System). Results were presented as the mean fluorescent intensity (MFI) of nuclear HMGB1 expression, normalized to untreated control cells.

Cytotoxicity of Cells after Treatment with HV(Mn^{2+}/Dox). The effect of HV(Mn^{2+}/Dox) on cell viability was ascertained by the cell counting kit-8 assay (CCK-8) (Dojindo Molecular Technologies, Inc., Kumamoto, Japan) according to the manufacturer's instructions. 4T1 and CT26 cells were exposed to 1 μg/mL of Mn^{2+}, 1 μg/mL of Dox, and both Mn^{2+}/Dox and 1 μg/mL of Dox in HV(Mn^{2+}/Dox) for 24 h. After the addition of 10% CCK-8 solution to each well, the cells were cultured for 2 h at 37 °C. The optical density was measured at 450 nm by a microplate reader.

Tumor-Targeting Study Using *In Vivo* Imaging System (IVIS). The tumor-targeting ability of HV particles was assessed using the near-infrared lipophilic DiR dye. HV particles were labeled with 19.7 μM DiR after the particle hybridization. Male BALB/c (6 weeks) were subcutaneously injected with 4×10^5 4T1 cells in the right flanks. DiR-labeled HV particles or free DiR dye was injected intravenously into the mice *via* the tail vein after tumors reached an average size of 200 mm^3. After 24 h post injection, fluorescence intensities were measured using an *in vivo* imaging system (IVIS Lumina imaging system, PerkinElmer). The average radiant efficiency was quantified from the acquired images.

***In Vivo* Antitumor Efficacy Studies.** Animals were cared for following federal, state, and local guidelines. All *in vivo* tests were in accordance with and approved by the University Committee on Use and Care of Animals (UCUCA) of the University of Michigan, Ann Arbor. Female BALB/c mice (5−6 weeks, Jackson Laboratories) were inoculated subcutaneously with CT26 cells (2×10^5 cells/mouse) or 4T1 cells (4×10^5 cells/mouse) on the right side of the flank to establish a single tumor model. The treatment groups included PBS, free Dox dosed at 2 mg/kg, free Mn^{2+} dosed at 2 mg/kg, and HV(Mn^{2+}/Dox) dosed at 2 mg/kg Dox equivalent. Treatments were initiated on day 6 post inoculation and were administered intravenously every 3 days for a total of 4 injections. The antitumor efficacy against CT26 or 4T1 cells was assessed by monitoring changes in tumor volume. The tumor volume (V) was calculated according to an ellipsoidal calculation, whereby $V = a \times b^2 \times 0.5$, where a is the largest and b is the smallest diameter of the tumor ellipsoid. At the indicated time point, bloods were collected from 4T1 tumor-bearing mice and sera were separated by centrifugation for biochemical analysis. Sera biochemical tests were analyzed in the Pathology Core of the University of Michigan. In the bilateral tumor model, mice were inoculated with 4×10^5 cells on the right flank and 2×10^5 cells on the left flank. Treatment commenced on day 6 post inoculation with the same regimens as the single tumor study. For the bilateral study, treatments were administered intratumorally every 3 days for a total of 4 injections, focusing on the right flank tumors. Both treated and untreated tumors were measured and recorded, as described above.

Statistical Analysis. The data are presented as mean ± standard error of the mean (SEM). Statistical comparisons were performed using unpaired Student's t-test for two-group comparisons, one-way analysis of variance (ANOVA) with Tukey's significant difference post hoc test for comparisons of more than three groups, or two-way analysis of variance (ANOVA) with Bonferroni post-tests or Tukey's significant difference post hoc test for comparisons of two independent variables using Prism 6 (GraphPad software). The differences were considered statistically significant when $p < 0.05$.

■ ASSOCIATED CONTENT

Supporting Information

The Supporting Information is available free of charge at https://pubs.acs.org/doi/10.1021/acsami.3c18569.

ELISA analysis of J774A.1 macrophages treated with LPS and IFN-γ; macrophage-targeting ability of HV(Mn^{2+}/Dox) by confocal microscopy; *in vitro* CXCR4 expression of cancer cell lines; cancer-targeting efficacy of HV(Mn^{2+}/Dox) *in vitro* by confocal microscopy; cancer-targeting efficacy of HV(Mn^{2+}/Dox) *in vitro* by flow cytometry; and comparative serum biochemical analyses of 4T1 tumor-bearing mice that received PBS or HV(Mn^{2+}/Dox) (PDF)

■ AUTHOR INFORMATION

Corresponding Authors

James J. Moon − *Department of Pharmaceutical Sciences, University of Michigan, Ann Arbor, Michigan 48109, United States; Biointerfaces Institute and Department of Biomedical Engineering, University of Michigan, Ann Arbor, Michigan 48109, United States;* orcid.org/0000-0003-2238-2372; Email: moonjj@umich.edu

Hansoo Park − *School of Integrative Engineering, Chung-Ang University, Seoul 06974, Republic of Korea;* orcid.org/0000-0002-3125-7680; Email: heyshoo@cau.ac.kr

Authors

Yeonwoo Jang − *School of Integrative Engineering, Chung-Ang University, Seoul 06974, Republic of Korea;* orcid.org/0000-0002-2144-9662

Young Seok Cho − *Department of Pharmaceutical Sciences, University of Michigan, Ann Arbor, Michigan 48109, United States; Biointerfaces Institute, University of Michigan, Ann Arbor, Michigan 48109, United States;* orcid.org/0000-0003-1338-3170

April Kim − *Department of Pharmaceutical Sciences, University of Michigan, Ann Arbor, Michigan 48109, United States*

Xingwu Zhou − *Department of Pharmaceutical Sciences, University of Michigan, Ann Arbor, Michigan 48109, United States;* orcid.org/0000-0001-5977-2185

Yujin Kim − *Department of Pharmaceutical Sciences, University of Michigan, Ann Arbor, Michigan 48109, United States; Biointerfaces Institute, University of Michigan, Ann Arbor, Michigan 48109, United States;* orcid.org/0000-0002-7186-221X

Ziye Wan − *Department of Pharmaceutical Sciences, University of Michigan, Ann Arbor, Michigan 48109, United States*

Complete contact information is available at:

https://doi.org/10.1021/acsami.3c18569
ACS Appl. Mater. Interfaces 2024, 16, 17129−17144

https://pubs.acs.org/10.1021/acsami.3c18569

Author Contributions

⊥Y.J. and Y.S.C. contributed equally to this work. J.J.M. and H.P. conceived the project and supervised the research. Y.J. was mainly responsible for conducting the experiments, performing the synthesis, analyzing the results, writing the manuscript, and preparing the figures. Y.S.C. was mainly responsible for the *in vivo* experiments, immunological analyses, data curation, and writing. A.K. revised the manuscript. X.Z. supported the *in vivo* experiments. Y.K. supported the preparation of materials. Z.W. supported the *in vivo* experiments. All authors participated in the editing of the manuscript and the discussion.

Notes

The authors declare no competing financial interest.

■ ACKNOWLEDGMENTS

This research was supported by the National Research Foundation of Korea (NRF) funded by the Ministry of Science and ICT (NRF-2021R1A2C2007189, NRF-2021R1A4A3025206) and Creative Materials Discovery Program through the National Research Foundation of Korea (NRF) funded by the Ministry of Science and ICT (NRF-2018M3D1A1058813). This work was also supported by the NIH (grant nos. R01AI127070, R01EB022563, R01CA210273, U01CA210152, R01DK125087, P30CA046592). J.J.M. was supported by an NSF CAREER Award (grant no. 1553831).

■ REFERENCES

(1) Esfahani, K.; Roudaia, L.; Buhlaiga, N.; Del Rincon, S.; Papneja, N.; Miller, W. H. A review of cancer immunotherapy: from the past, to the present, to the future. *Curr. Oncol.* **2020**, *27* (s2), 87−97, DOI: 10.3747/co.27.5223.

(2) Riley, R. S.; June, C. H.; Langer, R.; Mitchell, M. J. Delivery technologies for cancer immunotherapy. *Nat. Rev. Drug Discovery* **2019**, *18* (3), 175−196, DOI: 10.1038/s41573-018-0006-z.

(3) Yang, Y. Cancer immunotherapy: harnessing the immune system to battle cancer. *J. Clin. Invest.* **2015**, *125* (9), 3335−3337, DOI: 10.1172/JCI83871.

(4) Mokhtari, R. B.; Homayouni, T. S.; Baluch, N.; Morgatskaya, E.; Kumar, S.; Das, B.; Yeger, H. J. O. Combination therapy in combating cancer. *Oncotarget* **2017**, *8* (23), 38022−38043, DOI: 10.18632/oncotarget.16723.

(5) Emens, L. A.; Middleton, G. The interplay of immunotherapy and chemotherapy: harnessing potential synergies. *Cancer Immunol. Res.* **2015**, *3* (5), 436−443, DOI: 10.1158/2326-6066.CIR-15-0064.

(6) Chen, H.; Sha, H.; Zhang, L.; Qian, H.; Chen, F.; Ding, N.; Ji, L.; Zhu, A.; Xu, Q.; Meng, F.; et al. Lipid insertion enables targeted functionalization of paclitaxel-loaded erythrocyte membrane nanosystem by tumor-penetrating bispecific recombinant protein. *Int. J. Nanomed.* **2018**, *13*, 5347−5359, DOI: 10.2147/IJN.S165109.

(7) Hu, C.-M. J.; Fang, R. H.; Wang, K.-C.; Luk, B. T.; Thamphiwatana, S.; Dehaini, D.; Nguyen, P.; Angsantikul, P.; Wen, C. H.; Kroll, A. V.; et al. Nanoparticle biointerfacing by platelet membrane cloaking. *Nature* **2015**, *526* (7571), 118−121, DOI: 10.1038/nature15373.

(8) Guo, L.; Miao, Y.; Wang, Y.; Zhang, Y.; Zhou, E.; Wang, J.; Zhao, Y.; Li, L.; Wang, A.; Gan, Y.; Zhang, X. Biomimetic Macrophage Membrane and Lipidated Peptide Hybrid Nanovesicles for Atherosclerosis Therapy. *Adv. Funct. Mater.* **2022**, *32* (52), No. 2204822, DOI: 10.1002/adfm.202204822.

(9) Cho, Y. S.; Kim, H. R.; Park, S. J.; Chung, S. W.; Ko, Y. G.; Yeo, J. H.; Lee, J.; Kim, S. K.; Choi, J. U.; Kim, S. Y. J. B.; Byun, Y. Sustained potentiation of bystander killing via PTEN-loss driven macropinocytosis targeted peptide-drug conjugate therapy in metastatic triple-negative breast cancer. *Biomaterials* **2022**, *289*, No. 121783.

(10) Kim, H. R.; Cho, Y. S.; Chung, S. W.; Choi, J. U.; Ko, Y. G.; Park, S. J.; Kim, S. Y.; Byun, Y. Caspase-3 mediated switch therapy of self-triggered and long-acting prodrugs for metastatic TNBC. *J. Controlled Release* **2022**, *346*, 136−147, DOI: 10.1016/j.jconrel.2022.04.014.

(11) Xu, C.; Ju, D.; Zhang, X. Cell membrane-derived vesicle: A novel vehicle for cancer immunotherapy. *Front. Immunol.* **2022**, *13*, No. 923598, DOI: 10.3389/fimmu.2022.923598.

(12) Song, H.; Chen, X.; Hao, Y.; Wang, J.; Xie, Q.; Wang, X. Nanoengineering facilitating the target mission: Targeted extracellular vesicles delivery systems design. *J. Nanobiotechnol.* **2022**, *20* (1), No. 431, DOI: 10.1186/s12951-022-01638-9.

(13) Wang, Y.; Zhao, M.; Liu, S.; Guo, J.; Lu, Y.; Cheng, J.; Liu, J. disease. Macrophage-derived extracellular vesicles: Diverse mediators of pathology and therapeutics in multiple diseases. *Cell Death Dis.* **2020**, *11* (10), No. 924, DOI: 10.1038/s41419-020-03127-z.

(14) Xuan, M.; Shao, J.; Dai, L.; Li, J.; He, Q. interfaces. Macrophage cell membrane camouflaged Au nanoshells for in vivo prolonged circulation life and enhanced cancer photothermal therapy. *ACS Appl. Mater. Interfaces* **2016**, *8* (15), 9610−9618, DOI: 10.1021/acsami.6b00853.

(15) Lopes, J.; Lopes, D.; Pereira-Silva, M.; Peixoto, D.; Veiga, F.; Hamblin, M. R.; Conde, J.; Corbo, C.; Zare, E. N.; Ashrafizadeh, M.; et al. Macrophage Cell Membrane-Cloaked Nanoplatforms for Biomedical Applications. *Small Methods* **2022**, *6* (8), No. 2200289, DOI: 10.1002/smtd.202200289.

(16) Pan, Y.; Yu, Y.; Wang, X.; Zhang, T. Tumor-associated macrophages in tumor immunity. *Front. Immunol.* **2020**, *11*, No. 583084, DOI: 10.3389/fimmu.2020.583084.

(17) Boutilier, A. J.; Elsawa, S. F. Macrophage polarization states in the tumor microenvironment. *Int. J. Mol. Sci.* **2021**, *22* (13), No. 6995, DOI: 10.3390/ijms22136995.

(18) Mantovani, A.; Allavena, P.; Marchesi, F.; Garlanda, C. Macrophages as tools and targets in cancer therapy. *Nat. Rev. Drug Discovery* **2022**, *21* (11), 799−820, DOI: 10.1038/s41573-022-00520-5.

(19) Neupane, K. R.; McCorkle, J. R.; Kopper, T. J.; Lakes, J. E.; Aryal, S. P.; Abdullah, M.; Snell, A. A.; Gensel, J. C.; Kolesar, J.; Richards, C. I. Macrophage-engineered vesicles for therapeutic delivery and bidirectional reprogramming of immune cell polarization. *ACS Omega* **2021**, *6* (5), 3847−3857, DOI: 10.1021/acsomega.0c05632.

(20) Rayamajhi, S.; Nguyen, T. D. T.; Marasini, R.; Aryal, S. Macrophage-derived exosome-mimetic hybrid vesicles for tumor targeted drug delivery. *Acta Biomater.* **2019**, *94*, 482−494.

(21) Zhang, M.; Du, Y.; Wang, S.; Chen, B. A review of biomimetic nanoparticle drug delivery systems based on cell membranes. *Drug Des., Dev. Ther.* **2020**, *2020*, 5495−5503, DOI: 10.2147/DDDT.S282368.

(22) Jang, Y.; Kim, A.; Moon, J. J.; Lee, J. Y.; Park, H. Novel bioengineering strategies for drug delivery systems. *Appl. Mater. Today* **2023**, 33, No. 101834, DOI: 10.1016/j.apmt.2023.101834.

(23) Filippi-Chiela, E.; Solari, J. I.; Andrade, C.; Klamt, F.Damage-Associated Molecular Patterns (DAMPs) related to Immunogenic Cell Death are differentially triggered by clinically relevant chemotherapeutics in lung adenocarcinoma cells *BMC Cancer* 2019 DOI: 10.21203/rs.2.10439/v1.

(24) Florou, D.; Patsis, C.; Ardavanis, A.; Scorilas, A. therapy. Effect of doxorubicin, oxaliplatin, and methotrexate administration on the transcriptional activity of BCL-2 family gene members in stomach cancer cells. *Cancer Biol. Ther.* **2013**, *14* (7), 587−596, DOI: 10.4161/cbt.24591.

(25) Kawano, M.; Tanaka, K.; Itonaga, I.; Iwasaki, T.; Miyazaki, M.; Ikeda, S.; Tsumura, H. Dendritic cells combined with doxorubicin induces immunogenic cell death and exhibits antitumor effects for

osteosarcoma. *Oncol. Lett.* **2016**, *11* (3), 2169−2175, DOI: 10.3892/ol.2016.4175.
(26) Sun, X.; Zhang, Y.; Li, J.; Park, K. S.; Han, K.; Zhou, X.; Xu, Y.; Nam, J.; Xu, J.; Shi, X.; et al. Amplifying STING activation by cyclic dinucleotide−manganese particles for local and systemic cancer metalloimmunotherapy. *Nat. Nanotechnol.* **2021**, *16* (11), 1260−1270, DOI: 10.1038/s41565-021-00962-9.
(27) Li, J.; Ren, H.; Qiu, Q.; Yang, X.; Zhang, J.; Zhang, C.; Sun, B.; Lovell, J. F.; Zhang, Y. Manganese coordination micelles that activate stimulator of interferon genes and capture in situ tumor antigens for cancer metalloimmunotherapy. *ACS Nano* **2022**, *16* (10), 16909−16923, DOI: 10.1021/acsnano.2c06926.
(28) Hou, L.; Tian, C.; Yan, Y.; Zhang, L.; Zhang, H.; Zhang, Z. Manganese-based nanoactivator optimizes cancer immunotherapy via enhancing innate immunity. *ACS Nano* **2020**, *14* (4), 3927−3940, DOI: 10.1021/acsnano.9b06111.
(29) Zhang, K.; Qi, C.; Cai, K. Manganese-Based Tumor Immunotherapy. *Adv. Mater.* **2023**, *35* (19), No. 2205409, DOI: 10.1002/adma.202205409.
(30) Yao, Q.; Xu, C.; Zhao, H.; Chen, H. development; therapy. CXCR4 in breast cancer: oncogenic role and therapeutic targeting. *Drug Des., Dev. Ther.* **2015**, *2015*, 4953−4964, DOI: 10.2147/DDDT.S84932.
(31) Chittasupho, C.; Anuchapreeda, S.; Sarisuta, N. Biopharmaceutics. CXCR4 targeted dendrimer for anti-cancer drug delivery and breast cancer cell migration inhibition. *Eur. J. Pharm. Biopharm.* **2017**, *119*, 310−321, DOI: 10.1016/j.ejpb.2017.07.003.
(32) Brand, S.; Dambacher, J.; Beigel, F.; Olszak, T.; Diebold, J.; Otte, J.-M.; Göke, B.; Eichhorst, S. T. CXCR4 and CXCL12 are inversely expressed in colorectal cancer cells and modulate cancer cell migration, invasion and MMP-9 activation. *Exp. Cell Res.* **2005**, *310* (1), 117−130, DOI: 10.1016/j.yexcr.2005.07.006.
(33) Shin, H.-N.; Moon, H.-H.; Ku, J.-L. Stromal cell-derived factor-1α and macrophage migration-inhibitory factor induce metastatic behavior in CXCR4-expressing colon cancer cells. *Int. J. Mol. Med.* **2012**, *30* (6), 1537−1543, DOI: 10.3892/ijmm.2012.1141.
(34) Egorova, A.; Kiselev, A.; Hakli, M.; Ruponen, M.; Baranov, V.; Urtti, A. applications, i. c. Chemokine-derived peptides as carriers for gene delivery to CXCR4 expressing cells. *J. Gene Med.* **2009**, *11* (9), 772−781, DOI: 10.1002/jgm.1366.
(35) Guan, J.; Shen, Q.; Zhang, Z.; Jiang, Z.; Yang, Y.; Lou, M.; Qian, J.; Lu, W.; Zhan, C. Enhanced immunocompatibility of ligand-targeted liposomes by attenuating natural IgM absorption. *Nat. Commun.* **2018**, *9* (1), No. 2982, DOI: 10.1038/s41467-018-05384-1.
(36) Gong, C.; Yu, X.; You, B.; Wu, Y.; Wang, R.; Han, L.; Wang, Y.; Gao, S.; Yuan, Y. Macrophage-cancer hybrid membrane-coated nanoparticles for targeting lung metastasis in breast cancer therapy. *J. Nanobiotechnol.* **2020**, *18* (1), No. 92, DOI: 10.1186/s12951-020-00649-8.
(37) Abraham, S. A.; McKenzie, C.; Masin, D.; Ng, R.; Harasym, T. O.; Mayer, L. D.; Bally, M. B. In vitro and in vivo characterization of doxorubicin and vincristine coencapsulated within liposomes through use of transition metal ion complexation and pH gradient loading. *Clin. Cancer Res.* **2004**, *10* (2), 728−738, DOI: 10.1158/1078-0432.CCR-1131-03.
(38) Lee, C.; Liu, Q.-H.; Tomkowicz, B.; Yi, Y.; Freedman, B. D.; Collman, R. G. Macrophage activation through CCR5-and CXCR4-mediated gp120-elicited signaling pathways. *J. Leucocyte Biol.* **2003**, *74* (5), 676−682, DOI: 10.1189/jlb.0503206.
(39) Ma, Q.; Zhang, N.; You, Y.; Zhu, J.; Yu, Z.; Chen, H.; Xie, X.; Yu, H. Cardiology, C. CXCR4 blockade in macrophage promotes angiogenesis in ischemic hindlimb by modulating autophagy. *J. Mol. Cell. Cardiol.* **2022**, *169*, 57−70, DOI: 10.1016/j.yjmcc.2022.05.002.
(40) Sica, A.; Larghi, P.; Mancino, A.; Rubino, L.; Porta, C.; Totaro, M. G.; Rimoldi, M.; Biswas, S. K.; Allavena, P.; Mantovani, A. Macrophage polarization in tumour progression. *Seminars Cancer Biol.* **2008**, *18*, 349−355, DOI: 10.1016/j.semcancer.2008.03.004.
(41) Bianchi, M. E.; Mezzapelle, R. The chemokine receptor CXCR4 in cell proliferation and tissue regeneration. *Front. Immunol.* **2020**, *11*, No. 2109, DOI: 10.3389/fimmu.2020.02109.
(42) Cho, Y. S.; Kim, G. C.; Lee, H. M.; Kim, B.; Kim, H. R.; Chung, S. W.; Chang, H. W.; Ko, Y. G.; Lee, Y. S.; Kim, S. W.; et al. Albumin metabolism targeted peptide-drug conjugate strategy for targeting pan-KRAS mutant cancer. *J. Controlled Release* **2022**, *344*, 26−38, DOI: 10.1016/j.jconrel.2022.02.026.
(43) Deng, C.; Zhang, Q.; Jia, M.; Zhao, J.; Sun, X.; Gong, T.; Zhang, Z. Tumors and their microenvironment dual-targeting chemotherapy with local immune adjuvant therapy for effective antitumor immunity against breast cancer. *Adv. Sci.* **2019**, *6* (6), No. 1801868, DOI: 10.1002/advs.201801868.
(44) Gulen, M. F.; Koch, U.; Haag, S. M.; Schuler, F.; Apetoh, L.; Villunger, A.; Radtke, F.; Ablasser, A. Signalling strength determines proapoptotic functions of STING. *Nat. Commun.* **2017**, *8* (1), No. 427, DOI: 10.1038/s41467-017-00573-w.
(45) Galluzzi, L.; Buqué, A.; Kepp, O.; Zitvogel, L.; Kroemer, G. Immunogenic cell death in cancer and infectious disease. *Nat. Rev. Immunol.* **2017**, *17* (2), 97−111.
(46) Fan, Y.; Kuai, R.; Xu, Y.; Ochyl, L. J.; Irvine, D. J.; Moon, J. J. Immunogenic cell death amplified by co-localized adjuvant delivery for cancer immunotherapy. *Nano Lett.* **2017**, *17* (12), 7387−7393.
(47) Hansen, C. B.; Kao, G. Y.; Moase, E. H.; Zalipsky, S.; Allen, T. M. Attachment of antibodies to sterically stabilized liposomes: evaluation, comparison and optimization of coupling procedures **1995** *1239* 2133 144 DOI: 10.1016/0005-2736(95)00138-S.
(48) Alyane, M.; Barratt, G.; Lahouel, M. Remote loading of doxorubicin into liposomes by transmembrane pH gradient to reduce toxicity toward H9c2 cells. *Saudi Pharm. J.* **2016**, *24* (2), 165−175, DOI: 10.1016/j.jsps.2015.02.014.
(49) Abraham, S. A.; Edwards, K.; Karlsson, G.; MacIntosh, S.; Mayer, L. D.; McKenzie, C.; Bally, M. B. Formation of transition metal−doxorubicin complexes inside liposomes. *Biochim. Biophys. Acta, Biomembr.* **2002**, *1565* (1), 41−54, DOI: 10.1016/S0005-2736(02)00507-2.
(50) Lutz, M. B.; Kukutsch, N.; Ogilvie, A. L.; Rößner, S.; Koch, F.; Romani, N.; Schuler, G. An advanced culture method for generating large quantities of highly pure dendritic cells from mouse bone marrow. *J. Immunol. Methods* **1999**, *223* (1), 77−92, DOI: 10.1016/S0022-1759(98)00204-X.